nature COMMUNICATIONS

ARTICLE

DOI: 10.1038/s41467-017-02336-z OPEN

Broadband impedance match to two-dimensional materials in the terahertz domain

Phi H.Q. Pham[1], Weidong Zhang[2], Nhi V. Quach[1], Jinfeng Li[1], Weiwei Zhou[1], Dominic Scarmardo[1], Elliott R. Brown[2] & Peter J. Burke[1]

The coupling of an electromagnetic plane wave to a thin conductor depends on the sheet conductance of the material: a poor conductor interacts weakly with the incoming light, allowing the majority of the radiation to pass; a good conductor also does not absorb, reflecting the wave almost entirely. For suspended films, the transition from transmitter to reflector occurs when the sheet resistance is approximately the characteristic impedance of free space ($Z_0 = 377\,\Omega$). Near this point, the interaction is maximized, and the conductor absorbs strongly. Here we show that monolayer graphene, a tunable conductor, can be electrically modified to reach this transition, thereby achieving the maximum absorptive coupling across a broad range of frequencies in terahertz (THz) band. This property to be transparent or absorbing of an electromagnetic wave based on tunable electronic properties (rather than geometric structure) is expected to have numerous applications in mm wave and THz components and systems.

[1] Department of Electrical Engineering and Computer Science, University of California, Irvine, CA 92697, USA. [2] Department of Physics and Electrical Engineering, Wright State University, Dayton, OH 45435, USA. Correspondence and requests for materials should be addressed to P.J.B. (email: pburke@uci.edu)

Two-dimensional materials provide a class of atomically thin conductors[1–3] which can be synthesized with area much larger than the electromagnetic (EM) wavelength in the mm wave and THz bands, creating opportunities to control EM beams without the need for nanoscale patterning that is typically required in the optical[4, 5]. To date, unpatterned monolayer graphene devices have operated exclusively in the weakly coupled, highly transmissive regime[6–18].

Here, by deliberate engineering of the sheet conductance using large-domain graphene films in combination with chemically modified substrates (to decrease interface scattering), as well as chemical and electrical doping, we fabricate monolayer graphene devices with sheet resistance crossing the characteristic impedance of free space, 377 Ω/□ Achieving this, we show that monolayer graphene can be tuned to behave as a strong absorber over a broadband frequency range, approaching the theoretical impedance at which absorption is maximized[19, 20]. In free space, the maximum absorption is 50%, whereas on a substrate it can be greater than 90% depending on the direction of normal incidence, discussed in detail below. Regardless of the case (free space or on dielectric), the absorption is much larger than the 2.3% optical value[21], and thus represents a milestone of coupling electromagnetic waves to an atomically thin nanomaterial. This is measured over an extremely broad range, from mm wave to THz frequencies. Strong EM absorption using a single atomic layer exemplifies the fundamental relationship between nanoscale electronics and classical electromagnetism.

Results

THz conductance. The zero-gap band structure of graphene leads to a non-trivial frequency-dependent AC conductance, which governs the absorption of the EM radiation. As depicted in Fig. 1a, at optical frequencies the sheet conductance of graphene is dominated by interband transitions, and exhibits a universal value of $G_g = (\pi/4)\cdot G_0 = (e^2/4\hbar)$[21], where G_0 is the conductance quantum. This results in its low absorbance, approximated by the product of G_g and the characteristic impedance of free-space, Z_0 = 377 Ω. This product can be written $\pi\cdot(e^2/\hbar c) \equiv \pi\cdot\alpha$, where α is the fine structure = 1/137. Thus, only ≈ 2.3% of the light is absorbed, and the majority of the light is transmitted.

In contrast, at frequencies lower than ~ $2E_F/h$ (where E_F is the Fermi energy), as is the case in the THz range, the photon energy is too low to excite electron–hole pairs, and the electromagnetic sheet conductance is expected to follow the DC sheet conductance[22, 23]. This should occur for frequencies up to ~ $1/\tau$, where τ is the scattering time, at which point the conductance is expected to undergo a Drude-like roll-off[6–9], dropping towards the low optical value, (Fig. 1a). The AC conductance can be adjusted by engineering E_F and τ according to the equations:

$$G_{DC} = \frac{e^2}{4\hbar}\frac{4}{\pi}\frac{E_F\tau}{\hbar} \quad (1)$$

$$G(\omega) = \frac{G_{DC}}{1 + i\omega\tau} \quad (2)$$

This creates the opportunity to adjust the THz conductance into the regime where the majority of the incident light is absorbed ($A > R$, T). This prospect is indicated schematically within the THz frequency range in Fig. 1b, where hypothetical conductance curves for plausible E_F and τ values are plotted. Figure 1c presents "device design" charts (calculated for 100 GHz), which show how combinations of E_F and τ affect the AC conductance; the absorption-dominating regime begins when the sheet resistance ≤ 377 Ω/□ (set as red on the z-axis color scale). Previous investigations of single-layer graphene THz absorption fail to surpass the $Z_0 = 377$ Ω threshold[6–18] (denoted as circles in Fig. 1c), even in the case where E_F was designed to be purposefully large (using heavy chemical doping[6, 15], or strong electrical gating[6, 7, 10, 12, 13, 15]). Instead, as demonstrated in this work and emphasized as an arrow in Fig. 1d, by carefully fabricating devices with improved τ, the graphene conductance can be large (denoted as an 'x' in Fig. 1c), and the device sheet resistance can be tuned to be below the free space impedance threshold. We successfully surpass this threshold with a graphene sheet, and reach near maximum absorption.

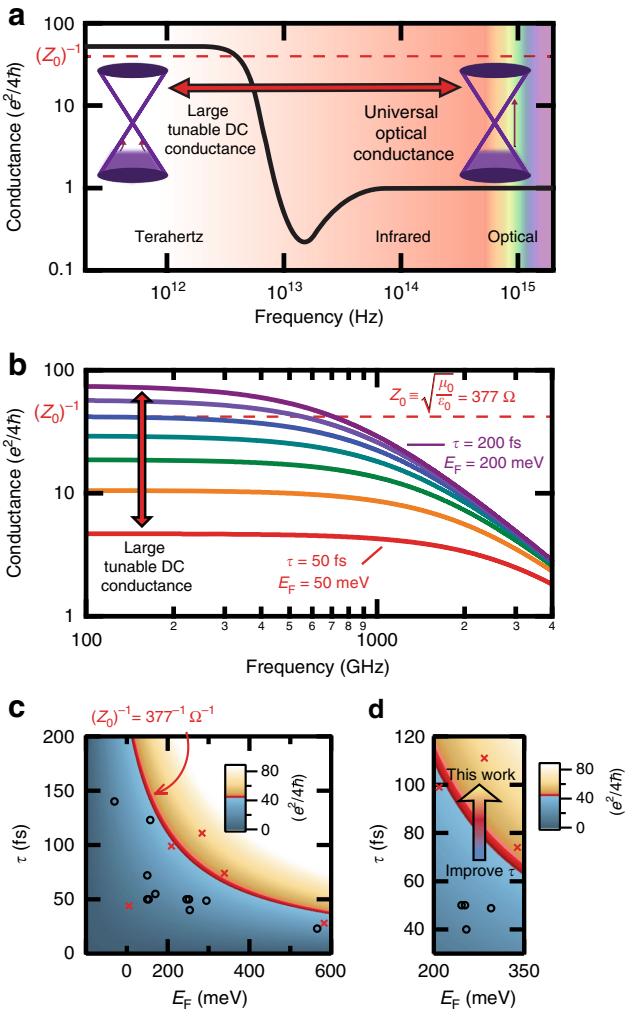

Fig. 1 THz conductance. **a** Qualitative trend of frequency-dependent AC conductance for monolayer graphene with normalization to $e^2/4\hbar$. The optical frequency range exhibits a universal value of 1, while in the THz range, the AC conductance can be orders of magnitude higher. **b** Theoretical trend of THz AC conductance for monolayer graphene plotted with a linear variation of the E_F, and τ. Graphene samples can cross the free space conductance value, $(Z_0)^{-1}$, within the THz regime. **c** Device design plot showing the graphene sheet conductance (at 100 GHz) in units of $(e^2/4\hbar)$ for changes in E_F and τ. The $(Z_0)^{-1}$ threshold is set as red on the color scale. Previous graphene THz device parameters are plotted as circles, whereas those from this work are denoted as x's. **d** By decreasing the electron scattering in our devices to increase τ, the $(Z_0)^{-1}$ threshold can be crossed into the absorption-dominating regime

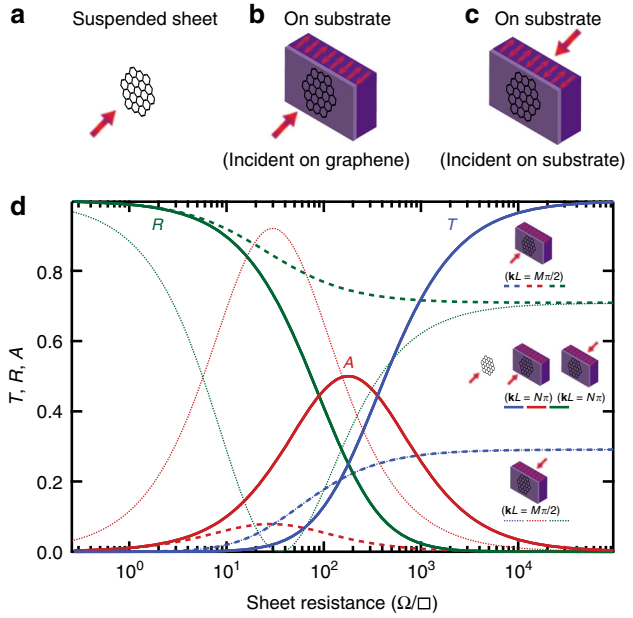

Fig. 2 Transmission, reflection and absorption. **a**–**c** A suspended film and a film on a substrate for two incidence directions were analyzed using the transmission line model. $n = 3.41$ was used as the substrate index of refraction for calculation. **d** The suspended film/Woltersdorff equations (plotted as solid lines) for T, R and A vs. sheet resistance were compared to a film on a substrate. When the half-wave resonance condition is satisfied ($\mathbf{k}L = N\pi$, where N is an integer), the equations for T, R and A reduce to exactly the Woltersdorff equations (plotted for both directions as solid lines, and are indistinguishable from the suspended film). Hence, analyzing the device at half-wave resonance provides a direct comparison of the graphene absorption on a substrate to that of a suspended film. At quarter-wave resonance ($\mathbf{k}L = M\pi/2$, where M is an odd integer), T is the same for both incidence directions, but R and A are different for each incidence direction (plotted as the dotted lines)

Transmission, reflection and absorption regimes. Our measurement technique consists of using an ultra-broadband THz spectrometer, based on the photomixing of two optical lasers to generate a coherent THz beam[24]. This system (block diagram shown in Supplementary Fig. 1) enables continuous transmission measurement from 200 GHz to 1.2 THz with over 60 dB dynamic range at the low end, and up to 40 dB at the high end. The graphene films are mounted on high-resistivity silicon substrates of thickness ~ 400 μm, which do not absorb significantly in the THz region. Because of the difference in the index of refraction between the silicon substrate ($n \approx 3.4$) and air ($n = 1$), there is an etalon effect present in the frequency-dependent transmission (even in the absence of graphene). With graphene present, we can model the effect of varying the graphene sheet resistance to calculate the net transmittance using the transmission line model (Supplementary Note 1–4), and compare these values (for a film on a substrate with incidence in both directions) to that of a suspended graphene film (Fig. 2a–c).

A plane wave can be transmitted (T), reflected (R) or absorbed (A). Electromagnetics states that a perfect conductor is a mirror ($T = 0$; $R = 1$; $A = 0$) and a perfect insulator is a transmitter ($T \leq 1$, $R \geq 0$, $A = 0$). What is the quantitative relationship between T, R, A and the sheet resistance? The three are not completely independent, as $T + R + A$ must equal unity due to conservation of energy. The relationship for the transmittance, reflectance, and absorptance of a suspended thin metallic film was derived in 1934[19], and is given by,

$$T = \frac{4g^2}{(1+2g)^2} \tag{3}$$

$$R = \frac{1}{(1+2g)^2} \tag{4}$$

$$A = \frac{4g}{(1+2g)^2} \tag{5}$$

$$g \equiv {}^{R}/_{Z_0} \tag{6}$$

These expressions show the change from transmission-dominating to absorption-dominating occurring at the critical threshold of $Z_0 = 377\,\Omega$. Within the absorption-dominating regime, the peak absorption occurs when the sheet resistance is equal to $Z_0/2$ (Fig. 2d).

When mounted on a substrate of index of refraction, n, numerous considerations such as direction of normal incidence (on the graphene or substrate side first) and substrate thickness govern T, R and A. Furthermore, interference effects from the substrate cause Fabry–Perot behavior depending on the THz frequency (f), substrate thickness (L) and index of refraction (n). When incident on the graphene side first, the general analytical expressions for T, R and A are given by,

$$T = 4Z_0\left|\frac{gn(n\sin(\mathbf{k}L) - i\cos(\mathbf{k}L))}{(1+g+gn^2)Z_0\sin(\mathbf{k}L) - i(1+2g)nZ_0\cos(\mathbf{k}L)}\right|^2 \frac{2Z_0}{1+n^2-\cos(2\mathbf{k}L)(n^2-1)} \tag{7}$$

$$R = \left|\frac{(1-g+gn^2)\sin(\mathbf{k}L) - in\cos(\mathbf{k}L)}{(1+g+gn^2)\sin(\mathbf{k}L) - i(1+2g)n\cos(\mathbf{k}L)}\right|^2 \tag{8}$$

$$A = 4gZ_0^2\left|\frac{\sin(\mathbf{k}L) - in\cos(\mathbf{k}L)}{(1+g+gn^2)Z_0\sin(\mathbf{k}L) - i(1+2g)nZ_0\cos(\mathbf{k}L)}\right|^2 \tag{9}$$

Similar expressions for incidence on the substrate side are given in Supplementary Note 4.

For both incidence directions, when $\mathbf{k}L = N\pi$, where $\mathbf{k}$, is the wave vector, L is the substrate thickness, and N is integer values, or when the THz frequency is at half-wave resonance with the graphene–silicon etalon, which occurs at even integer multiples of $f = \frac{c}{(4*n*L)}$, the equations for T, R and A reduce to exactly the same as the Woltersdorff equations[19] (Eqs. 3–5). Hence, for a broadband transmittance measurement, at half-wave resonance, or at the transmittance maxima (up to a critical sheet resistance value, after which the half-wave resonance occurs at the transmittance minima, see Supplementary Note 3 and Supplementary Fig. 4e), the behavior of the graphene film can be directly compared to a suspended film, where the onset of strong absorption occurs at $Z_0 = 377\,\Omega$, with maximum absorption of 50% occurring at $Z_0/2$. In Fig. 2d the half-wave resonance condition for T, R and A are indistinguishable from those of the suspended case.

In contrast, at quarter-wave resonance, when $\mathbf{k}L = M\pi/2$, where M is odd integer values, the sheet resistance-dependent

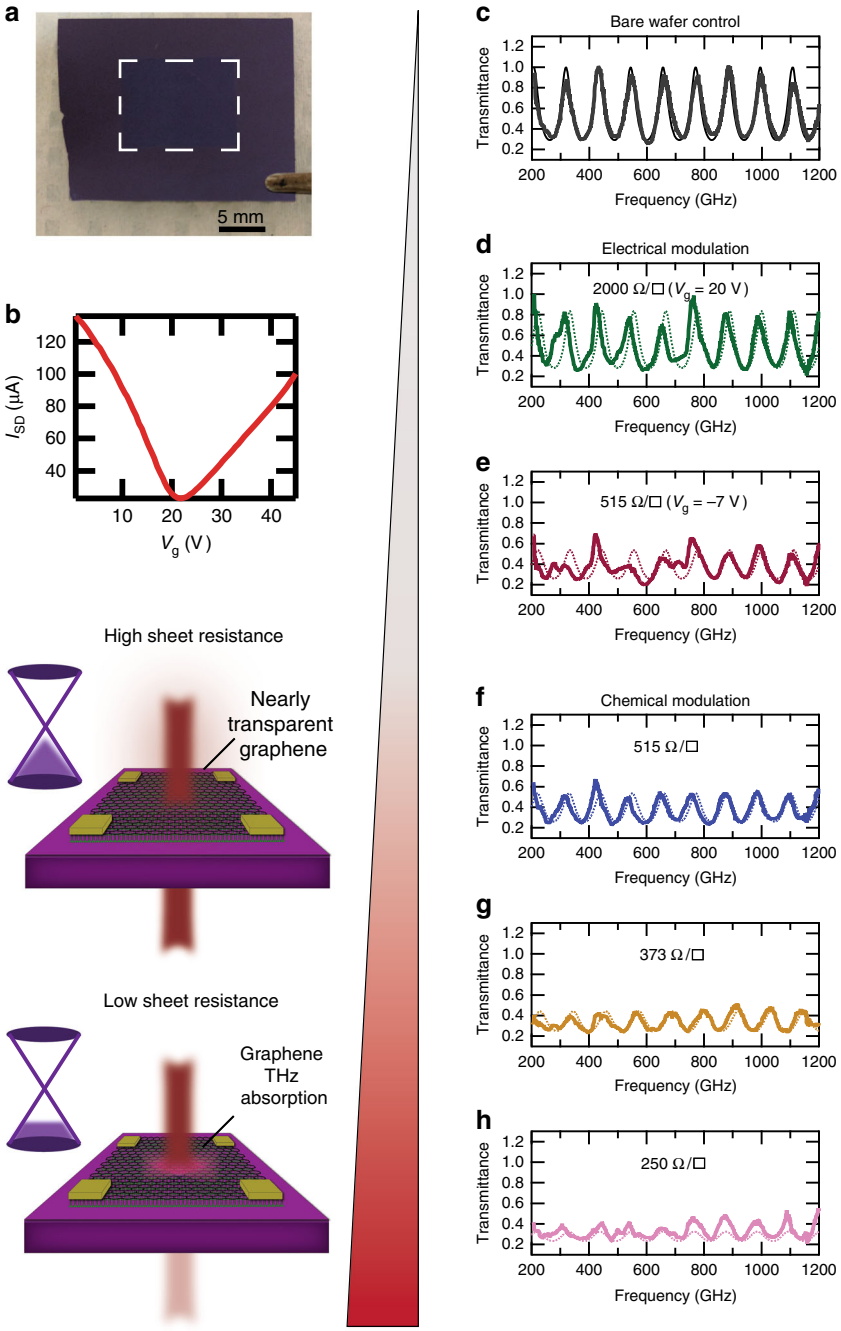

Fig. 3 Broadband impedance matching. **a** Optical photograph of graphene transferred onto ODTS modified oxide on high-resistivity silicon substrate. The scale bar is ~ 5 mm. **b** Source-drain current vs. gate voltage for typical graphene on ODTS SAM device. The charge neutral point is ~ 22 V. **c** Transmittance vs. frequency data acquired for a control sample (bare high-resistivity silicon substrate with no graphene). **d**, **e** Transmittance vs. frequency data for a graphene sample gated at 20 V and −7 V. **f**–**h** Transmittance vs. frequency for three devices after chemical doping to modify the zero-bias sheet resistance. The expected transmittance values assuming the DC conductance as the AC contribution (assuming negligible susceptance) are plotted as dotted lines

transmission through the graphene–silicon etalon remains low (transmission never dominates). Although the transmittance is low and equivalent for both incidence directions (graphene or substrate first), the sheet resistance-dependent reflection and absorption indeed depend on the incidence direction. When the THz beam is incident on the graphene side first, interference effects cause the device to behave as mostly reflecting (always reflection dominating), resulting in low absorption. On the other hand, when the THz beam is incident on the substrate first (with graphene on the backside), the absorption, transmission and reflection can be affectedly tuned by the sheet resistance. This allows the absorption maximum to increase to > 50% for low sheet resistance values (Supplementary Fig. 5a).

The two extreme cases (half-wave resonance and quarter-wave resonance) shows contrasting behavior, but like the suspended film, there still exists certain impedance values that determine the peak absorption, and the onset of the absorption-dominating threshold (Fig. 2d). The absorption-dominating threshold and peak absorption can shift (to even lower sheet resistance values) depending on the substrate index of refraction. We have calculated and plotted this trend for various values of the index of refraction in Supplementary Fig. 5b. Regardless of whether the

graphene film is suspended or on a substrate, the largest sheet resistance value (most resistive) in which the film becomes absorption dominating is 377 Ω/□, and hence this value signifies the doorway to strong absorption. Detailed below, we observe a decrease in the broadband transmittance as the graphene sheet resistance is tuned below 377 Ω/□, signifying absorption approaching the 50% maximum for a THz beam incident on a graphene sheet on substrate.

Graphene device fabrication on modified substrate. Previously, researchers used bare, unpatterned graphene, and measured the THz resistance to be greater than 377 Ω[6–18]. This includes our previous work[9], where the graphene–etalon structures were fabricated using chemical vapor-deposited graphene films[25] transferred[26] onto a 90 nm gate oxide layer on high-resistivity silicon substrates. To improve τ, so as to increase the conductance of the devices, we synthesized large-domain (mm-sized) graphene films (to minimize graphene grain boundaries)[27], in addition to depositing octadecyltrichlorosilane (ODTS) self-assembled monolayers (SAM) on the wafer (to decrease scattering)[28] prior to graphene transfer (Supplementary Note 5). Across the measured frequency range, the SAM does not significantly affect the THz absorption (Supplementary Note 6). The resulting air/graphene/substrate structure shown in Fig. 3a was used for THz transmission measurements with the THz beam incident on the graphene side first. When gating the graphene to the charge neutral point (CNP) without the use of a SAM, large voltages (> 50 V) must be applied to the high-resistivity silicon layer. Utilization of the SAM layer provides significant improvement of the transconductance of the graphene film, and a smaller operating voltage window (Supplementary Fig. 7b–c). The depletion curve shown in Fig. 3b shows a CNP at ~ 22 V, and indicates slight *p*-doping of the graphene film. We performed a series of THz transmission measurements on these devices for a variety of sheet resistance values, as shown in Fig. 3d–h.

Electrical modulation of broadband THz. In order to deconvolve the etalon effect, the broadband transmission through a bare high-resistivity silicon substrate (without graphene) is first measured as a control. The multiple interference peaks of transmission around ≈ 1.0 (Fig. 3c) confirm the low-loss nature of the bare substrate. Upon the addition of a monolayer sheet of graphene on the ODTS SAM buffer layer (and when applying a voltage on the silicon substrate near the V_{CNP} (≈ 20 V) as shown in Fig. 3d), the graphene film behaves as a nearly transparent film (sheet resistance ≈ 2 kΩ/□), as the amplitudes of the transmission peaks approach unity. The theoretical graphene-on-Si etalon transmittance vs frequency curves, calculated for an AC admittance that is purely real (susceptance equal to zero) and equal to the measured DC conductance, are plotted as dotted lines for comparison, and generally agree with the measured values. This is clearly in the transmission-dominating regime, as the presence of the graphene has little effect on the THz transmission through the sample.

We next demonstrate the ability to electrically tune to the absorption-dominating regime. By applying −7 V, the graphene DC sheet resistance is decreased to ≈ 515 Ω/□, and we observe considerably decreased maxima in the transmission peaks (Fig. 3e). Despite the fact that the gate voltage drop across the graphene film is small compared to the high-resistivity silicon substrate, consistent with the *I*–*V* curve (Fig. 3b), our device still enables significant control of the single-layer graphene sheet resistance, which results in a large transmittance variation of the incident THz radiation. The gate-modified transmittance peak values are plotted together with the *I*–*V* characteristics in Supplementary Fig. 8a for an additional device. Gate leakage through the oxide and ODTS SAM ([10^{-5}] A) was observed at voltages beyond this range, and hence gate voltages were restricted to −7 V to +45 V. Across the broadband frequency range measured, the transmittance variation at the peaks can be used to define a depth of modulation (DoM) (relevant to the use as a spatial-light modulator), defined as $(T_{High}-T_{Low})/T_{High}$. The DoM is substantial, with a maximum value of ≈ 52% at the ~ 330 GHz peak (Supplementary Fig. 8b). For a simple, unpatterned device geometry, consisting of only one monolayer, this is the largest transmittance variation that has been reported to date for a graphene-based modulator, to the best of our knowledge[9, 10, 12, 15, 17]. A 52% DoM is comparable to other patterned graphene devices such as extraordinary optical transmission structures[29] and periodic arrays of graphene nanodisks[30]. Compared to patterned device geometries, which usually create frequency- or polarization-dependent behavior, our device structure (which does not require any lithography) allows for useful THz modulation over 1 THz of frequency range with polarization independence. This result was independently confirmed in two different labs (Supplementary Note 7).

Impedance matching using chemical doping. Figure 4a shows the inferred frequency-dependent conductance varying from much less than $(Z_0)^{-1}$ (green curve, V_g = +20 V, 10× less than $(Z_0)^{-1}$), to approximately equal to $(Z_0)^{-1}$ (red curve, V_g = −7 V), and clearly demonstrates electrical tuning from the transmission to absorption-dominating regimes. In order to achieve the necessary sheet conductance values near maximum absorption, and beyond $(Z_0)^{-1}$, we utilized chemical (rather than electrical) tuning. We intentionally dope graphene films to have low sheet resistance in the zero-bias state (to mitigate inconsistencies that may arise from the inhomogeneous gating using a high-resistivity substrate, and to ensure no gate leakage occurs) by using benzimidazole (BI) dissolved into the copper etching solution during graphene transfer[31] (Supplementary Note 8). Figure 3f–h shows the broadband transmittance vs. frequency for three graphene films having zero-bias DC sheet resistances of 515, 373 and 250 Ω/□, respectively. Similar to the electrical modulation, we observe a steady decrease in the THz transmittance peaks. The lowest sheet resistance is clearly less than 377 Ω and the trend of reduced transmission with reduced sheet resistance is observed over the entire measurement band.

Drude conductance and strong absorption. The measured transmission spectra can be used to determine the AC sheet conductance, using the bare silicon control sample as nearly lossless "calibration"[9] (although it is noted that the transmission peaks do not necessarily remain at a fixed frequency when covered by a thin film). For devices covered by a graphene film, each transmittance peak is fitted to yield a AC admittance (real conductance and imaginary susceptance) value; the measured DC conductance and the estimated THz conductance are then fitted according to Eqs. 1 and 2 to estimate E_F and τ for each device (Supplementary Note 9). The calculated peak conductance values are shown in Fig. 4a, b, with a dotted red line showing the 377 Ω threshold. The predicted Drude conductance using the estimated E_F and τ is plotted as a solid line, and closely matches the measured DC value (shown on the *y*-axis). Supplementary Note 10 summarizes in a graphical representation our achievement crossing the free-space impedance threshold within the mm wave and THz frequency ranges, and compares our data to previous measurements in the literature. In this work, the frequency-domain measurement is especially broad (spanning the sub-THz regime), and the optical conductance and THz absorption of the

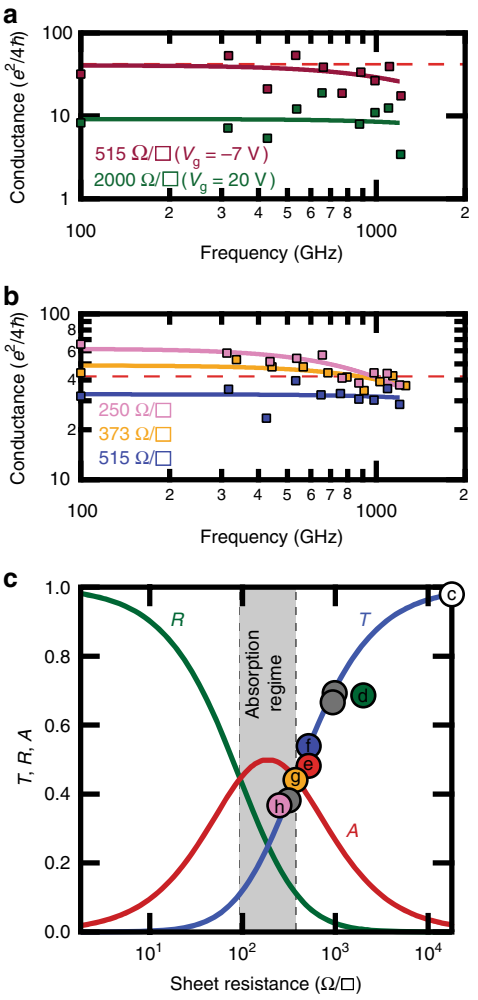

Fig. 4 Drude conductance and strong absorption. **a**, **b** The AC conductance values calculated by fitting the measured transmittance peaks for both electrically and chemically modified devices from Fig. 3 are plotted as squares. Drude model trends estimated from the frequency-dependent AC conductance data are plotted as solid lines. **c** The measured transmittance peak values (at ~ 655 GHz) are plotted as a function of sheet resistance. Colored (labeled) circles represent data from devices shown above, gray circles are from devices measured, but not displayed in Fig. 3, and the white circle represents the control sample. The theoretical transmittance, absorbance and reflectance values calculated from the half-wave resonance case for a device on a substrate are plotted as solid lines. The transmittance value becomes less than the absorbance value at sheet resistance values < 377 Ω/□, marking the beginning of the absorption regime

graphene film are remarkably large for one atomic layer. Supplementary Table 1 shows the extracted Drude parameters, E_F and τ, for measured devices. Notably, the values of E_F are moderate, while the values of τ can be large (> 100 fs), and stress the importance of engineering τ, as initially outlined in the device design plots in Fig. 1c, d. These figures clearly demonstrate our ability to tune the sheet resistance of monolayer graphene, either electrically or chemically, from well above to below the characteristic impedance of free space. We next focus on our more quantitative demonstration of the relationship between the transmittance and the sheet resistance.

We plot in Fig. 4c the predicted transmission (blue line), reflection (green line) and absorption (red line) for a graphene film as a function of sheet resistance for a film mounted on a silicon substrate, at half-wave resonance satisfying the condition $\mathbf{k}L = N\pi$. At half-wave resonance, the free-space and etalon effect give the same predicted T, R and A vs. sheet resistance (Fig. 2). We also show the measured transmittance peak (centered around ~ 655 GHz) values (color points are from devices measured in Fig. 3, gray points are for devices measured during this work, but not displayed in Fig. 3). The 377 Ω vertical dotted line indicates the characteristic impedance of free-space threshold, and marks the start of the absorption regime, where the fractional absorbance (~ 0.44) of the THz radiation by the graphene film becomes greater than the fractional transmittance (and reflectance)[19]. Here, we have realized the crossover from the transmission regime, and have measured correspondingly small transmittance values for devices within the absorption regime. For our best single-layer device of ≈ 250 Ω/□, the value of the graphene film absorbance is calculated to be ≈ 48.6%: approaching the theoretical limit of 50% (for normal incidence on graphene side first).

Discussion

Instead of designing the single-layer sheet resistance to cross into the absorption-dominating regime, previous experiments for unpatterned graphene devices boosted low absorbance by the addition of multilayers[32–35], or by suppressing the transmission channel[36] using double-pass/reflection/"Salisbury screen" geometries[11, 14]. Other thin film (multilayer) materials have also demonstrated remarkable control of absorption by controlling film thickness, such as niobium nitride (NbN)[37–39] and indium tin oxide (ITO)[40]. Here, our experiments show that exceptionally large, near maximum, absorption can be reached in the thickness limit of one single layer of graphene.

Impedance matching to the free-space threshold using a double-pass, reflection mode geometry could achieve 100% absorption[34, 41], and may further enhance the single-layer reflection DoM[11, 42]. Pertaining to designing devices that operate in transmission (such as the work performed here), the suspended film and Woltersdorff equations[19] stand as the ideal situation for broadband absorption. Using the transmission line model for a film on a substrate, as the substrate index of refraction value approaches $n = 1$, or the substrate thickness approaches, $L = 0$, the amplitudes of the Fabry–Perot fringes decrease, and the widths of the fringes increase (as calculated values converge toward the suspended film/Woltersdorff equations for all frequencies). Although it is shown by calculation[43] that the (quarter-wave resonance) absorption can be greater than 50% if the THz beam is incident on the substrate side first (Supplementary Note 11), this geometry does not easily allow for use as a transmission-mode modulator, because changes in the sheet resistance have less effect on the transmittance compared to the geometry employed in our experiments. Nevertheless, it could still be useful as a reflection-mode device, but the major challenge of engineering low sheet resistance values remains, since absorption greater than 80% in this geometry requires sheet resistance values of less than 100 Ω/□.

We were able to achieve a large transmission DoM by improving the transconductance (allowing the sheet resistance of a single device to span a broad range) of the graphene on ODTS SAM layer. The high-quality, large-domain graphene films on SAM used here were confirmed via Raman mapping[44, 45] (Supplementary Note 8), and suggest that substrate modification improves the sheet resistance by improving mobility at high carrier density[28, 46] (Supplementary Fig. 15). Although other materials can exhibit tunable conductance such as vanadium dioxide (VO_2)[47–49], NbN[37–39], ITO[40], metal thin films or even multilayer graphite, the conductance of monolayer graphene can be easily tuned via external voltages due to the extremely high

mobility. For high-frequency applications, the mobility of single-layer graphene is superior to bilayer (multilayer) graphene[50], and other semiconducting materials[42, 51], but fabrication remains a challenge for large-area devices which precludes electronically tunable devices operating at very low sheet resistance (even in the simple case of EM incidence on the substrate side first). A combination of substrate modification to improve mobility with techniques such as electrolyte gating[33] or device integration[17] could yield electrically controlled devices with high modulation frequency and low operation voltage (see Supplementary Note 7). Additional improvements in large-area (mm-scale) graphene synthesis and transfer will foster better control from the transmission-to-absorption regimes (towards the reflection-dominating regime), as recent reports on large-area CVD graphene demonstrate mobility values as large as 350,000 ($cm^2 V^{-1} s^{-1}$) with sheet resistance spanning ~ ($e^2/4\hbar$) to 500($e^2/4\hbar$) at DC applying only ~ 5 V_g[52]. Our studies reveal the opportunity for a device based on the tunable electronic properties, without complicated fabrication steps required for other THz modulation schemes such as metamaterials[29, 30, 53], nanophotonic resonators[54], thin film thickness tuning[37–40, 47] or materials with switchable metal-to-insulator phase transitions[47–49].

We have demonstrated that the control of the large-area graphene DC sheet resistance enables the tuning, either electrically or chemically, from the transmission to absorption-dominating regimes at mm wave to THz frequencies. This could have wide-ranging application in the tunable and controllable manipulation of mm wave and THz light, including, for example, gate tunable THz modulators, electronically steerable phased array antennas and radar and tunable variable focus lenses and cones. However, while we have clearly demonstrated a single layer tuned from the transmission to absorption regimes (the gray shaded region in Fig. 4c where $A > T, R$), we have not pushed well below the inflection point between poor to excellent conductor (the lower bound in Fig. 4c where $R > T, A$). Future work with increased conductivity (e.g., by improved materials synthesis, using other two-dimensional materials other than graphene, etc) may enable complete tuning from strong transmitter, to strong absorber, to strong reflector, and would enable new technologies to manipulate EM radiation in powerful ways.

Methods

CVD graphene growth. Fully continuous monolayer graphene films are grown on copper foils (Alfa Aesar 94555) via chemical vapor deposition (CVD) in a 5-inch-diameter quartz tube. Large-domain (mm-scale grain boundaries) graphene films are synthesized using a fast, oxygen-assisted growth using two stages of methane flow (0.8 and 2.4 sccm flow rates) to separate nucleation and edge growth as presented in ref. [27]. All gases are left flowing until the furnace cools to less than 300 °C. The entire CVD process occurs with the quartz tube evacuated by a dry scroll pump.

ODTS SAM deposition. High-resistivity Si wafers with a 90-nm-thick, gate-quality SiO_2 layer on top are cleaned in hot piranha solution for 1 h followed by cleaning in deionized (DI) water. The wafers are placed in a vacuum chamber with 50 µL of ODTS solution in a glass vial. The chamber is then pumped down and the ODTS is allowed to self-assemble on the SiO_2 surface for 6 h.

Graphene transfer. Graphene covering a copper foil (≈ 1 cm^2) is coated with poly (methyl methacrylate) (PMMA) solution and etched in 5% ammonium persulfate (APS) solution. The floating PMMA/graphene stack is washed in DI water and wet transferred onto the substrate. For BI doping experiments, BI (0.03 M) was dissolved in a solution of APS, H_2SO_4 and H_2O_2 for copper etching. This process simultaneously etches the copper and dopes the graphene as described in ref. [31]. Following transfer, the wafer is dried overnight. Before PMMA removal, the wafer is heated on a hotplate at 130 C for 30 min. After cooling to room temperature, the wafer is placed in an acetone bath for 24 h for PMMA removal. The wafers are finally rinsed with isopropyl alcohol, and dried with N_2 gas.

Electrical characterization of graphene devices. To probe the electrical properties of the transferred graphene films, four Cr/Au (20/50 nm) electrodes were deposited by electron beam deposition using a shadow mask. All devices use the same shadow mask to maintain a consistent area to be measured. The electrodes were deposited in a square geometry with ≈ 5 mm gap separation between each electrode. The current between two diagonally opposed electrodes, representing the drain and source electrodes, was measured with 100 mV bias applied. Gate voltages were applied through the SiO_2 layer, with sweeps between −7 and 45 V (experimentally determined window to avoid leakage). Sheet resistance measurements were performed using a lock-in amplifier and a 4-point van der Pauw method.

THz characterization. An Emcore PB7200 broadband frequency-domain photomixing spectrometer was used to perform THz transmission measurements through the graphene-on-Si etalon structures. As shown in Supplementary Fig. 1, one photomixer acts as a THz transmitter, and a separate photomixer as a THz receiver; one of two distributed feedback lasers is tuned by temperature to perform the broadband difference frequency sweep between 0.2 and 1.2 THz with a 500 MHz step[24]. An aperture was placed between the sample and the THz beam to ensure that the THz beam area (≈ 3 mm diameter) was consistent from sample to sample, and less in area than the graphene film. The THz beam was then aligned at the geometric center of the four electrodes on the graphene film.

Theoretical calculations. The trend lines according to Eqs. 1 and 2 in Fig. 1b are plotted using a linear variation in τ, and E_F from 50 fs, and 50 meV, to 200 fs and 200 meV (with a step size of 25 fs and 25 meV), respectively. Figure 1c, d plots the conductance value at 100 GHz varying τ, and E_F from 0.5 fs, and 0.5 meV, to 200 fs and 600 meV (with a step size of 0.5 fs and 0.5 meV), respectively.

The transmittance vs. frequency plots for various sheet resistances (dotted lines) in Fig. 3c–h were calculated using the transmission line model as in ref.[40]. The model assumes quasi-plane wave radiation, substrate index of refraction $n = 3.41$ and the graphene sheet is treated as a shunt, lumped impedance, Z_g, where the real part of the graphene impedance (admittance) is equal to the measured DC resistance (conductance), assuming negligible imaginary contributions. The substrate thickness was inputted accordingly during calculation, and variations from device to device are listed in Supplementary Note 12.

The fitting of measured transmittance data follows our previous work as described in ref.[9]. To calculate the AC conductance data points (Fig. 4a, b) the transmission matrix method was performed using a least-mean-squares fit procedure (Supplementary Note 5). For each data point, one transmission peak and two neighboring valleys were used to calculate the admittance (Supplementary Note 13). The thickness of the substrate was varied accordingly for each device (Supplementary Note 12).

The fitting for trend lines in Fig. 4a, b use Eqs. 1 and 2 and a least-means-squares fitting procedure consisting of the real part of the calculated AC conductance values, and the measured DC value to estimate E_F and τ for each device. Up to the final fitting procedure (to estimate E_F and τ), all data fitting consisted of both real and imaginary contributions.

Data availability. The data that support the findings of this study are available from the corresponding author upon request.

Received: 12 July 2017 Accepted: 22 November 2017
Published online: 20 December 2017

References

1. Fiori, G. et al. Electronics based on two-dimensional materials. *Nat. Nanotechnol.* **9**, 768–779 (2014).
2. Chhowalla, M. et al. The chemistry of two-dimensional layered transition metal dichalcogenide nanosheets. *Nat. Chem.* **5**, 263–275 (2013).
3. Butler, S. Z. et al Progress, challenges, and opportunities in two-dimensional materials beyond graphene. *ACS Nano* **7**, 2898–2926 (2013).
4. Bonaccorso, F., Sun, Z., Hasan, T. & Ferrari, A. C. Graphene photonics and optoelectronics. *Nat. Photonics* **4**, 611–622 (2010).
5. Koppens, F. H. L. et al. Photodetectors based on graphene, other two-dimensional materials and hybrid systems. *Nat. Nanotechnol.* **9**, 780–793 (2014).
6. Yan, H. et al. Infrared spectroscopy of wafer-scale graphene. *ACS Nano* **5**, 9854–9860 (2011).
7. Horng, J. et al. Drude conductivity of Dirac fermions in graphene. *Phys. Rev. B* **83**, 165113 (2011).
8. Rouhi, N. et al. Terahertz graphene optics. *Nano Res.* **5**, 667–678 (2012).
9. Zhang, W., Pham, P. H. Q., Brown, E. R. & Burke, P. J. AC conductivity parameters of graphene derived from THz etalon transmittance. *Nanoscale* **6**, 13895–13899 (2014).
10. Sensale-Rodriguez, B. et al. Broadband graphene terahertz modulators enabled by intraband transitions. *Nat. Commun.* **3**, 780 (2012).

11. Sensale-Rodriguez, B. et al. Extraordinary control of terahertz beam reflectance in graphene electro-absorption modulators. *Nano Lett.* **21**, 936–941 (2012).
12. Ren, L. et al. Terahertz and infrared spectroscopy of gated large-area graphene. *Nano Lett.* **12**, 3711–3715 (2012).
13. Cervetti, C. et al. Sub-terahertz frequency-domain spectroscopy reveals single-grain mobility and scatter influence of large-area graphene. *Adv. Mater.* **27**, 2635–2641 (2015).
14. Min Woo, J., Kim, M.-S., Woong Kim, H. & Jang, J.-H. Graphene based salisbury screen for terahertz absorber. *Appl. Phys. Lett.* **104**, 81106 (2014).
15. Maeng, I. et al. Gate-controlled nonlinear conductivity of dirac fermion in graphene field-effect transistors measured by terahertz time-domain spectroscopy. *Nano Lett.* **12**, 551–555 (2012).
16. Buron, J. D. et al. Graphene mobility mapping. *Sci. Rep.* **5**, 12305 (2015).
17. Liang, G. et al. Integrated terahertz graphene modulator with 100% modulation depth. *ACS Photonics* **2**, 1559–1566 (2015).
18. Mics, Z. et al. Thermodynamic picture of ultrafast charge transport in graphene. *Nat. Commun.* **6**, 7655 (2015).
19. Woltersdorff, W. Uber die optischen Konstanten dunner Metallschichten im langwelligen Ultrarot. *Z. fur Phys.* **91**, 230–252 (1934).
20. Sten, J. C. E. & Koivisto, P. K. Optimum transparent absorbers of electromagnetic waves. *IEEE Trans. Electromagn. Compat.* **50**, 1011–1014 (2008).
21. Nair, R. R. et al. Fine structure constant defines visual transparency of graphene. *Science* **320**, 1308 (2008).
22. Gusynin, V. P., Sharapov, S. G. & Carbotte, J. P. On the universal ac optical background in graphene. *New J. Phys.* **11**, 95013 (2009).
23. Falkovsky, L. A. Optical properties of graphene and IV–VI semiconductors. *Phys.-Uspekhi* **51**, 887 (2008).
24. Demers, J. R., Logan, R. T. & Brown, E. R. An optically integrated coherent frequency-domain THz spectrometer with signal-to-noise ratio up to 80 dB. In *2007 International Topical Meeting on Microwave Photonics* (Ed. Darcie, T.E.) 92–95 (IEEE, 2007).
25. Li, X. et al. Large-area synthesis of high-quality and uniform graphene films on copper foils. *Science* **324**, 1312–1314 (2009).
26. Suk, J. W. et al. Transfer of CVD-grown monolayer graphene onto arbitrary substrates. *ACS Nano* **5**, 6916–6924 (2011).
27. Pham, P. H. Q. et al. Controlling nucleation density while simultaneously promoting edge growth using oxygen-assisted fast synthesis of isolated large-domain graphene. *Chem. Mater.* **28**, 6511–6519 (2016).
28. Lee, W. H. et al. Control of graphene field-effect transistors by interfacial hydrophobic self-assembled monolayers. *Adv. Mater.* **23**, 3460–3464 (2011).
29. Gao, W. et al. High-contrast terahertz wave modulation by gated graphene enhanced by extraordinary transmission through ring apertures. *Nano. Lett.* **14**, 1242–1248 (2014).
30. Fang, Z. et al. Active tunable absorption enhancement with graphene nanodisk arrays. *Nano. Lett.* **14**, 299–304 (2014).
31. Kim, S. J. et al. Simultaneous etching and doping by Cu-stabilizing agent for high-performance graphene-based transparent electrodes. *Chem. Mater.* **26**, 2332–2336 (2014).
32. Batrakov, K. et al. Enhanced microwave-to-terahertz absorption in graphene. *Appl. Phys. Lett.* **108**, 123101 (2016).
33. Balci, O., Polat, E. O., Kakenov, N. & Kocabas, C. Graphene-enabled electrically switchable radar-absorbing surfaces. *Nat. Commun.* **6**, 6628 (2015).
34. Wu, B. et al. Experimental demonstration of a transparent graphene millimetre wave absorber with 28% fractional bandwidth at 140 GHz. *Sci. Rep.* **4**, 4130 (2014).
35. Grande, M. et al. Optically transparent microwave polarizer based on quasi-metallic graphene. *Sci. Rep.* **5**, 17083 (2015).
36. Thongrattanasiri, S., Koppens, F. H. L. & Garcia De Abajo, F. J. Complete optical absorption in periodically patterned graphene. *Phys. Rev. Lett.* **108**, 47401 (2012).
37. Gorshunov, B. P., Fedorov, I. V., Kozlov, G. V., Volkov, A. A. & Semenov, A. D. Dynamic conductivity and the coherence peak in the submillimeter spectra of superconducting NbN films. *Solid State Commun.* **87**, 17–21 (1993).
38. Gorshunov, B. P. et al. Measurement of electrodynamic parameters of superconducting films in the far-infrared and submillimeter frequency ranges. *Int. J. Infrared Millim. Waves* **14**, 683–702 (1993).
39. Pronin, A. V. et al. Direct observation of the superconducting energy gap developing in the conductivity spectra of niobium. *Phys. Rev. B* **57**, 14416–14421 (1998).
40. Brown, E. R., Zhang, W. D., Chen, H. & Mearini, G. T. THz behavior of indium-tin-oxide films on p-Si substrates. *Appl. Phys. Lett.* **107**, 91102 (2015).
41. Sensale-Rodriguez, B. et al. Exceptional tunability of THz reflectance in graphene structures. In *2012 37th International Conference on Infrared, Millimeter, and Terahertz Waves* (Eds Lewis, R. A. & Zhang, C.) 1–3 (IEEE, 2012).
42. Sensale-Rodriguez, B. et al. Unique prospects for graphene-based terahertz modulators. *Appl. Phys. Lett.* **99**, 113104 (2011).
43. Zanotto, S. et al. Coherent absorption of light by graphene and other optically conducting surfaces in realistic on-substrate configurations. *APL Photonics* **2**, 16101 (2017).
44. Ferrari, A. C. et al. Raman spectrum of graphene and graphene layers. *Phys. Rev. Lett.* **97**, 187401 (2006).
45. Das, A. et al. Monitoring dopants by Raman scattering in an electrochemically top-gated graphene transistor. *Nat. Nanotechnol.* **3**, 210–215 (2008).
46. Rakheja, S., Kumar, V. & Naeemi, A. Evaluation of the potential performance of graphene nanoribbons as on-chip interconnects. *Proc. IEEE* **101**, 1740–1765 (2013).
47. Dressel, M. & Gruner, G. *Electrodynamics of Solids: Optical Properties of Electrons in Matter* (Cambridge University Press, Cambridge, 2002).
48. Verleur, H. W., Barker, A. S. & Berglund, C. N. Optical properties of VO2 between 0.25 and 5 eV. *Rev. Mod. Phys.* **172**, 788 (1968).
49. Liu, M. et al. Terahertz-field-induced insulator-to-metal transition in vanadium dioxide metamaterial. *Nature* **487**, 345–8 (2012).
50. Dean, C. R. et al. Boron nitride substrates for high-quality graphene electronics. *Nat. Nanotechnol.* **5**, 722–726 (2010).
51. Wang, L. One-dimensional electrical contact to a two-dimensional material. *Science* **342**, 614–617 (2013).
52. Banszerus, L. et al. Ultrahigh-mobility graphene devices from chemical vapor deposition on reusable copper. *Sci. Adv.* **1**, e1500222 (2015).
53. Rahm, M., Li, J. S. & Padilla, W. J. THz wave modulators: a brief review on different modulation techniques. *J. Infrared Millim. Terahertz Waves* **34**, 1–27 (2013).
54. Majumdar, A., Kim, J., Vuckovic, J. & Wang, F. Graphene for tunable nanophotonic resonators. *IEEE J. Sel. Top. Quantum Electron* **20**, 68–71 (2014).

Acknowledgements

We appreciate the conversations with D. Fishman, J. Hes and D. Humphrey. SEM and oxygen plasma work was performed at the Irvine Materials Research Institute (IMRI). Raman spectroscopy work was performed at the UC Irvine Laser Spectroscopy Facility (LSF). CVD synthesis and e-beam evaporation was performed at the Integrated Nano-systems Research Facility (INRF). This work was funded by the Army Research Office through the ARO-MURI Program and an ARO-Core Grant (Contract No: W911NF-11-1-0024 and W911NF-09-1-0319).

Author contributions

P.H.Q.P., W. Zhang, E.R.B. and P.J.B. conceived the experiments. P.H.Q.P., N.V.Q., W. Zhou and D.S. fabricated the devices. P.H.Q.P., N.V.Q. and W. Zhang performed material characterization and THz measurements. P.H.Q.P., W. Zhang, J.L., E.R.B. and P. J.B. performed theoretical calculations and fitting. P.H.Q.P., W. Zhang, E.R.B. and P.J.B. wrote the manuscript.

Additional information

Supplementary Information accompanies this paper at https://doi.org/10.1038/s41467-017-02336-z.

Competing interests: The authors declare no competing financial interest.

Reprints and permission information is available online at http://npg.nature.com/reprintsandpermissions/

Publisher's note: Springer Nature remains neutral with regard to jurisdictional claims in published maps and institutional affiliations.

Supplementary Information

Broadband THz Spectrometer

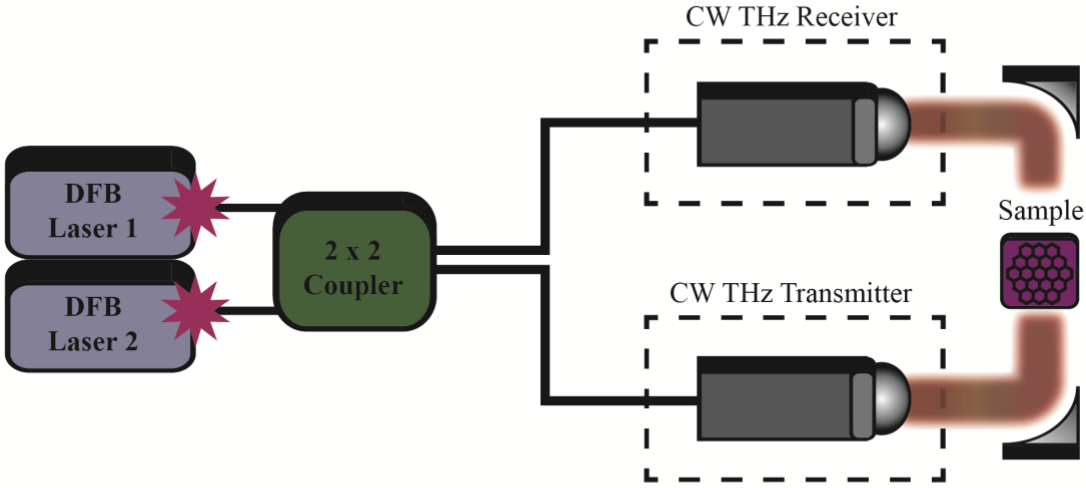

Supplementary Figure 1: Block diagram of the Emcore PB7200 broadband frequency-domain photomixing spectrometer used to perform THz transmission measurements through the graphene-on-Si etalon structures. Two distributed feedback lasers (DFB) are mixed in order to perform broadband frequency sweeps between 0.2 – 1.2 THz with 500 MHz steps.

Supplementary Note 1 - Impedance, Resistance, Conductance

In circuits, impedance means the ratio of the voltage across a given element to the current through a given element, and can be complex (i.e. the current and voltage may be out of phase). An "element" is a physical object with dimensions much smaller than the wavelength at the frequency of interest. The resistance, reactance, admittance, susceptance, and conductance all are various representations of the real or imaginary part of the impedance or its inverse. However, in our experiments, there are no "elements" (all of our structures are of order the wavelength in size), hence one must consider the electromagnetics of waves, not lumped elements.

In electromagnetic waves, the wave impedance means the ratio of the electric field to the magnetic field, and can also be complex (i.e. the electric field and magnetic field may be out of phase). This is also sometimes referred to as the characteristic impedance or the wave impedance of the medium. In cases where the medium is not lossy, the electric field and magnetic field are in phase, and hence the wave impedance is purely real. For example, in vacuum, the wave impedance is 377 Ω. Even though there is no imaginary component, one still generally refers to this as the "characteristic impedance of free space". For all of our experiments, the medium is not absorbing and so the wave impedance is always real. In a medium with index of refraction n (assuming n real as is the case for our experiments), the wave impedance (or also called the characteristic impedance of the medium) is given by 377 Ω/n. Note that a similar definition holds for

the characteristic impedance of a transmission line, which is a distributed inductance and capacitance (and perhaps conductance).

In the context of conducting media such as a metal, the wave impedance has significant imaginary components. In this case, the wave impedance is referred to as the "surface impedance",[1] even for cases where the waves are propagating and there is no physical "surface" in sight. We avoid this definition of "surface impedance" as it does not directly apply to our case.

Instead, we use the concept of sheet resistance. The sheet resistance of a thin film is the ratio of the voltage through a film of width W and length L to the current through that film, divided by the number of squares, i.e. L/W. The concept of sheet impedance is similar; if the voltage and current are out of phase the sheet impedance can have an imaginary component. The sheet conductance is defined similarly. While we consider the case of an imaginary component in the supplementary info for our experiments, we find little evidence for it experimentally in our frequency range and so the main text focuses the sheet resistance only.

The purpose of this paper is to show that, when a plane wave is incident on a thin film, the transmission, reflection, and absorption coefficients of that plane wave depend on the ratio of the characteristic impedance of the wave to the sheet resistance of the thin film.

The quantitative calculation of the transmission, reflection, and absorption coefficients is simplified dramatically using a transmission line equivalent circuit model that captures the key electromagnetic wave phenomena but requires only the use of discreet or disturbed circuit elements, and is described in detail. The model was validated theoretically and experimentally[2].

Supplementary Note 2 - Transmission Line Model

To analyze the THz transmittance of metallic films on dielectric substrates, a transmission-line model can provide accurate values of the transmittance, absorptance, and reflectance over a wide frequency range[2]. The primary requirement is that the incident beam be much wider in extent than the thickness of the substrate + metallic film, and that the beam be at, or near, a "waist". The secondary requirement is that the metallic film be much thinner than a wavelength, which is quite easy to satisfy in the THz region. The "waist" condition means that the constant-phase surface for the beam is a plane perpendicular to the direction of propagation. Hence, because the transmittance depends heavily on the interference effects of propagation in the film + substrate structure, the propagation can be handled as a transverse electromagnetic (TEM) mode. And TEM modes are the basis of the transmission-line model. From a practical standpoint, it is actually more realistic than the standard "plane-wave" model in physical optics because the latter assumes the beam has not only a planar constant-phase surface but also infinite lateral extent - something impossible to achieve in real optical systems.

The equivalent-circuit diagram of the transmission-line model is shown in **Supplementary Fig. 2b**. The incident beam is modelled as a TEM ideal voltage source

having phasor amplitude v_s and source resistance η_0 - the intrinsic impedance of free space. The thin-film-on -substrate structure is represented by the parallel combination of a complex impedance Z_G and a possibly lossy transmission line (to account for substrate absorption effects) of characteristic impedance Z_0. The free space region after the structure is represented by the free-space intrinsic (load) resistance η_0.

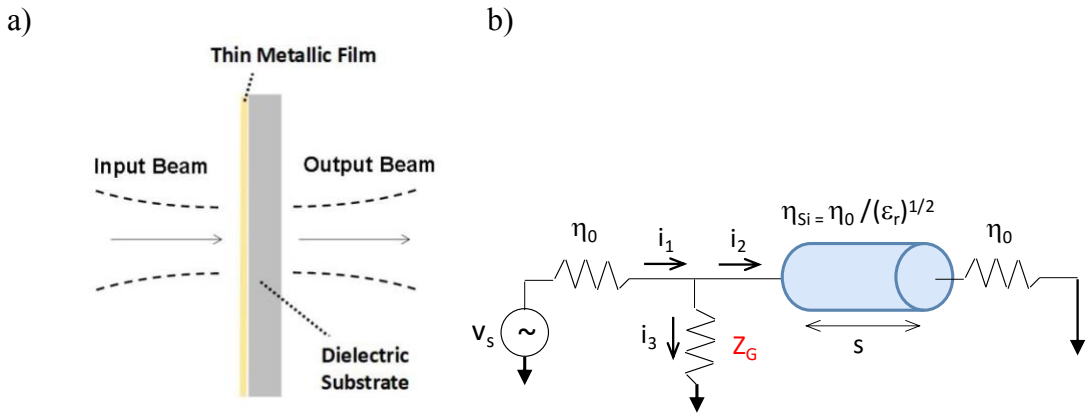

Supplementary Figure 2: a) Beam propagation through a thin metallic film on substrate b) Transmission-line equivalent-circuit model

The combination of transmission line plus free load resistance can be written

$$\eta(s) = \eta_s[\eta_0 + \eta_s \cdot \tanh(\gamma \cdot s)]/[\eta_s + \eta_0 \cdot \tanh(\gamma \cdot s)] \quad (1)$$

where s is the substrate thickness and γ is the complex propagation constant, and η_s is the intrinsic impedance of the substrate = $\eta_0/(\varepsilon_r)^{1/2}$. **Supplementary Eq. (1)** comes from the basic theory of lossy TEM transmission lines such that $\eta(s)$ represents the complex impedance "seen" by a generator connected to the input port[3].

Given the circuit in **Supplementary Fig. 2b**, we can calculate the transmitted power, the power dissipated in the thin-film-on-substrate structure, and the reflected power as follows. We first calculate the phasor currents flowing out of the generator i_1, into the transmission line i_2, and into the thin film i_3, where $i_1 = i_2 + i_3$ by the Kirchoff current law. By voltage division, we then have

$$i_1 = \frac{v_s}{\eta_0 + Z_G \,||\, \eta(s)}, \quad i_2 = i_1 \frac{Z_G}{Z_G + \eta(s)}; \text{ and } \quad i_3 = i_1 \frac{\eta(s)}{Z_G + \eta(s)} \quad (2)$$

where the last two follow from current division. Substitution for i_1 then yields

$$i_2 = \frac{v_s}{\eta_0 + Z_G \,||\, \eta(s)} \frac{Z_G}{Z_G + \eta(s)} \quad (3)$$

and,

$$i_3 = \frac{v_s}{\eta_0 + Z_G \,||\, \eta(s)} \frac{\eta(s)}{Z_G + \eta(s)}. \quad (4)$$

The average power dissipated in the thin-film-on-substrate structure is (assuming Ohm's law and sinusoidal phasor)

$$P_2 = \frac{1}{2}|i_2|^2 \,\mathrm{Re}\{\eta(s)\} = \frac{1}{2}|v_s|^2 \left| \frac{1}{\eta_0 + Z_G \,||\, \eta(s)} \frac{Z_G}{Z_G + \eta(s)} \right|^2 \cdot \mathrm{Re}\{\eta(s)\} \tag{5}$$

and the transmittance T through the metal film is just P_2 divided by the "available power" from the source, $|v_s|^2/8\eta 0$. Hence, we can write

$$T = \frac{1}{2}|i_2|^2 \,\mathrm{Re}\{\eta(s)\} = 4\eta_0 \cdot \left| \frac{1}{\eta_0 + Z_G \,||\, \eta(s)} \frac{Z_G}{Z_G + \eta(s)} \right|^2 \cdot \mathrm{Re}\{\eta(s)\} \tag{6}$$

By similar reasoning the average power dissipated in Z_G is

$$P_3 = \frac{1}{2}|i_3|^2 \,\mathrm{Re}\{Z_G\} = \frac{1}{2}|v_s|^2 \left| \frac{1}{\eta_0 + Z_G \,||\, \eta(s)} \frac{\eta(s)}{Z_G + \eta(s)} \right|^2 \cdot \mathrm{Re}\{Z_G\} \tag{7}$$

Such that the thin film absorptance is

$$A = \frac{1}{2}|i_3|^2 \,\mathrm{Re}\{Z_G\} = 4\eta_0 \cdot \left| \frac{1}{\eta_0 + Z_G \,||\, \eta(s)} \frac{\eta(s)}{Z_G + \eta(s)} \right|^2 \cdot \mathrm{Re}\{Z_G\} \tag{8}$$

By conservation of energy (and power), the reflectance is just

$$R = 1 - T - A \tag{9}$$

This set of equations can handle a wide variety of materials and conditions which are difficult to calculate by conventional (i.e., plane-wave) propagation techniques.

Special Case#1: No Substrate; Purely Resistive Film

The lack of a substrate is the simplest case since according to **Supplementary Eq. (1)** and the behavior of the tanh function, $\eta(s) \rightarrow \eta(s=0) = \eta_0$. Substitution into (6) then yields,

$$T = 4\eta_0^2 \cdot \left| \frac{1}{\eta_0 + (Z_G\eta_0)/(Z_G + \eta_0)} \frac{Z_G}{Z_G + \eta_0} \right|^2 = 4\eta_0^2 \cdot \left| \frac{Z_G}{\eta_0^2(1 + 2Z_G/\eta_0)} \right|^2 \tag{10}$$

substitution into (8) yields,

$$A = 4\eta_0^3 R_G \cdot \left| \frac{1}{\eta_0^2(1 + 2Z_G/\eta_0)} \right|^2 \tag{11}$$

and substitution into (9) yields

$$R = 1 - 4\eta_0^2(\eta_0 R_G + |Z_G|^2) \left| \frac{1}{\eta_0^2(1 + 2Z_G/\eta_0)} \right|^2 \tag{12}$$

In the special case of a resistive film, $Z_G = R_G$, **Supplementary Eq. (10) - (12)** can be greatly simplified algebraically:

$$T = \frac{4R_G^2/\eta_0^2}{(1 + 2R_G/\eta_0)^2} \tag{13}$$

$$A = \frac{4R_G/\eta_0}{(1+2R_G/\eta_0)^2} \tag{14}$$

$$R = \frac{1}{(1+2R_G/\eta_0)^2} \tag{15}$$

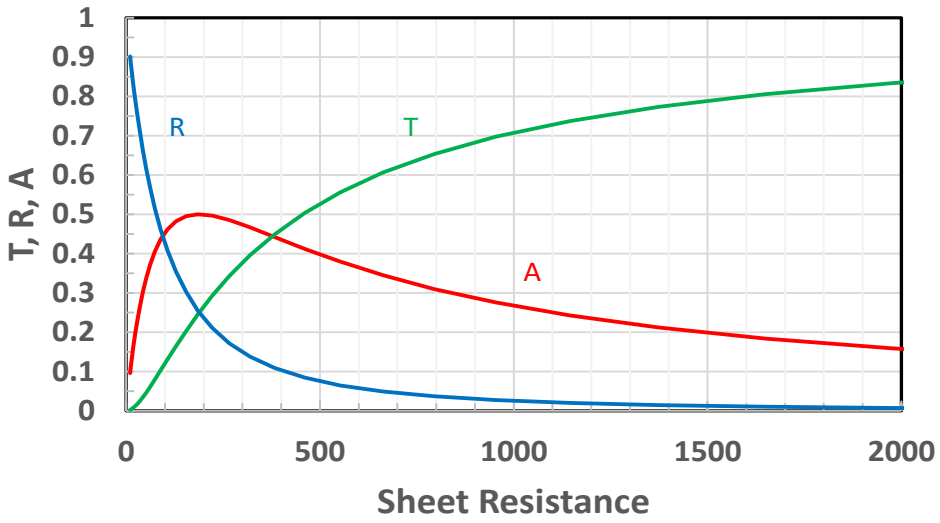

Supplementary Figure 3: The T, R, A values versus sheet resistance for a suspended, purely resistive film.

Interestingly none of these depends on frequency unless R_G is dispersive (more on that later). Historically, **Supplementary Eq. (14)** is known as the Wolsterdorff equation[4].

To check on the physical reasonableness of these last three equations, we note that in the limit of $R_G \to 0$ (thick metal or "ideal conductor"), T =0, A =0, and R =1 , i.e., we have the "perfect mirror". In the limit, $R_G \to \infty$ (infinitesimal metal or "ideal insulator"), T =1, A =0, and R =0, i.e., we have the "perfect transmitter". In the special case $R_G \to \eta_0$, we have T = 4/9, A = 4/9, and R = 1/9. Plots of **Eq. (13) - (15)** vs R_G are shown in **Supplementary Fig. 3**. The value of R_G that maximizes A is $R_G = \eta_0/2$ for which T=1/4, A=1/2, and R=1/4. For all values of R_G, T + A + R = 1, consistent with conservation of power.

Special Case#2: Lossless Substrate; Purely Resistive Film

Because of the difficulty of suspending thin metal films in free space, a more practical case is a substrate of finite thickness but negligible loss. This can be readily achieved even in the THz region by highly-resistive substrates having zero or very low polarity, such as high-resistivity silicon. The low polarity is necessary to make the optical phonons weakly interacting with electromagnetic radiation (silicon having near-zero polarity). In this case, we can re-write **Supplementary Eq. (1)** as

$$\eta(s) = \eta_s[\eta_0 + i\eta_s \cdot \tan(\gamma \cdot s)]/[\eta_s + i\eta_0 \cdot \tan(\gamma \cdot s)] \tag{16}$$

which is the familiar expression from microwave engineering textbooks. Because $\eta_s \neq \eta_0$, substitution into **Supplementary Eq. (6), (8), (10)** then creates a distinct frequency dependence consistent with the well-known behavior of transmission lines that are not

impedance matched to their load. But there are special cases well known from microwave transformer theory that simplify the analysis once again.

For a "half-wave" transformer, $\gamma \cdot s = m(2\pi/\lambda)\cdot\lambda/2 = m\pi$, where m is any integer (including zero) and λ is the wavelength in the transmission-line medium having dielectric constant ε_r, and index of refraction, $n = (\varepsilon_r)^{1/2}$. This condition makes $\tan(\gamma \cdot s) \rightarrow 0$ for all m, so according to **Supplementary Eq. (16)**, $\eta(s) = \eta_0$. And then we recover the same values of T, A, and R, as given by **Supplementary Eq. (13) - (15)**. For a given s, the half-wave condition is satisfied by a set of periodic frequencies $\nu = m \cdot c/(2ns)$, where m = any positive integer (including zero). For a "quarter-wave" transformer, $\gamma \cdot s = (2\pi/\lambda)*\lambda/4 = \pi$, so that $\tan(\gamma s) \rightarrow \infty$, and $\eta(s) = (\eta_s)^2/\eta_0$.

Supplementary Note 3 - Transmission Line Model for Calculating T, R, A

Using the transmission line model, the effect of different substrate dielectric constant/index of refraction can be easily accounted for, and provides a convenient "device design tool". For our experiments where graphene is mounted on a silicon substrate, $\varepsilon_s \approx 11.66$, and a substrate thickness of L = 400 μm is used for the calculations of T, R, and A. These values are compared to a suspended film, and a graphene film on substrate in **Supplementary Fig. 4**. In order to investigate the frequency dependence, in the figure below, the scattering time is set as, τ = 50 fs, as this value is widely reported in the literature (see table below). On half-wave resonance (~ 110 GHz for L = 400 μm), which occur at even integer multiples of $f = \frac{c}{(4*n*L)}$, or when $kL = N\pi$, the transmittance, reflectance, absorptance values from the transmission line model reduce to the Woltersdorff[4] values. In contrast, at odd integer multiples $f = \frac{c}{(4*n*L)}$, the device is at quarter-wave resonance (~ 164 GHz for L = 400 μm), and mostly reflecting. The equations for T, R, A are listed below. For device design, in the limit where the substrate index of refraction n = 1, and thickness of L = 0, the frequency dependent Fabry-Perot fringes of T, A, R decrease in amplitudes, and approaches the ideal case of a suspended film where the T, R, A values are generally flat with broadband, 50% absorption, matching the Woltersdorff values.

Half-Wave Resonance at Transmittance Peak

It is important to note that, even though the transmission line model matches the Woltersdorff values at the half-wave resonance values (**Supplementary Fig. 4d,h**), the half-wave resonance condition does not always occur at a transmittance peak maxima. The half-wave resonance condition occurs at a transmittance maxima up to a certain critical sheet resistance value (i.e. when the sheet resistance is large), but because of a phase shift when the graphene film becomes reflecting (i.e. when the sheet resistance value is small), the half-wave resonance condition occurs at the transmittance minima[2]. This phenomenon is obvious in **Supplementary Fig. 4e**; for sheet resistance values greater than 156 Ω/sq, the half-wave resonance condition occurs at the transmittance maxima, but for sheet resistance values less than 156 Ω/sq, the half-wave resonance condition occur at the transmittance minima. In this work, we never reach this critical sheet resistance threshold, and thus, in the manuscript, the half-wave resonance condition is referred to at the transmittance peak maxima. The opposite situation occurs for quarter-

wave resonance, that is, for high sheet resistance the quarter-wave resonance occurs at a transmittance minima, but after the critical sheet resistance is reached, the quarter-wave resonance flips and occurs at the transmittance maxima.

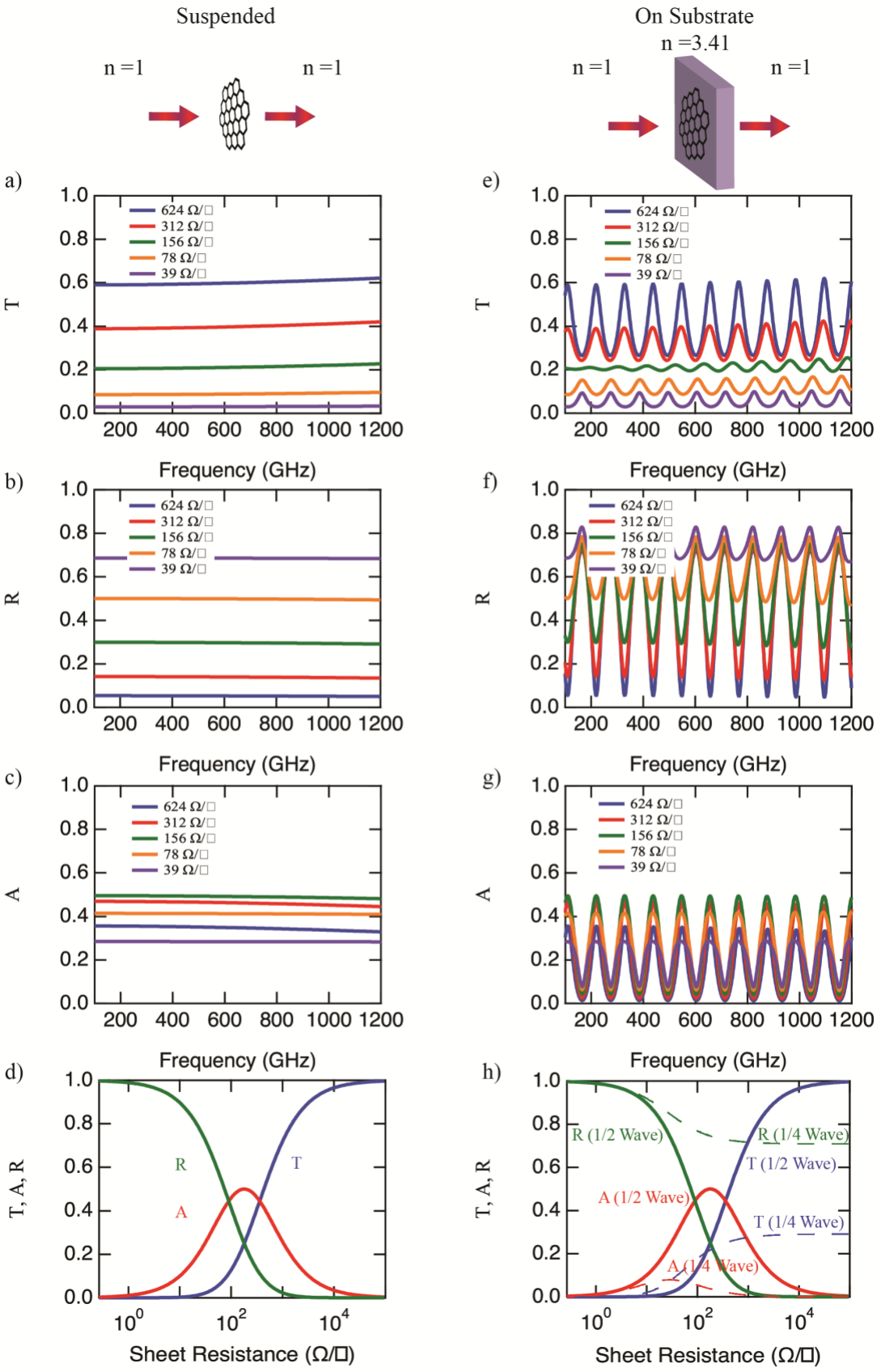
Suspended
On Substrate
n =3.41
n =1
n =1
n =1
n =1
a)
e)
b)
f)
c)
g)
d)
h)
T
R
A
T, A, R
624 Ω/□
312 Ω/□
156 Ω/□
78 Ω/□
39 Ω/□
Frequency (GHz)
Sheet Resistance (Ω/□)
R (1/2 Wave)
R (1/4 Wave)
T (1/2 Wave)
T (1/4 Wave)
A (1/2 Wave)
A (1/4 Wave)

Supplementary Figure 4: Two scenarios were analyzed to investigate the effects of the index of refraction of the substrate used in this work: suspended graphene films, and graphene on a substrate of finite thickness (n = 3.41, L = 400 um) with the THz beam incident on the graphene film first. a-c) The frequency dependent T, A, R was calculated for a suspended film for various assumed values of the DC sheet resistance. d) The single frequency T, A, R values for a suspended film as the sheet resistance is varied. e-g) The frequency dependent T, A, R was calculated for a film on a substrate, using the transmission line model for various assumed values of the DC sheet resistance. At the half-wave resonance, the amplitudes of the transmittance match those of the suspended sheet. h) The half-wave resonance, and quarter-wave resonance values for T, A, R are plotted as the sheet resistance is varied.

Theoretical T, R, A for Suspended Film (Woltersdorff[4])

$$A = \frac{4\,(R_{\square}/Z_0)}{(1+\frac{R_{\square}}{Z_0/2})^2} \qquad A = \frac{4\,g}{(1+2g)^2} \tag{17, 20}$$

$$R = \frac{1}{(1+\frac{R_{\square}}{Z_0/2})^2} \qquad R = \frac{1}{(1+2g)^2} \tag{18, 21}$$

$$T = \frac{1}{(1+\frac{Z_0/2}{R_{\square}})^2} \qquad T = \frac{4g^2}{(1+2g)^2} \tag{19, 22}$$

Quarter-Wave Resonance Case (Incident on Graphene)

$$A = \frac{4\,R_{\square}Z_0}{|R_{\square}n + R_{\square} + Z_0|^2} \tag{23}$$

$$R = \left|1 - \frac{2R_{\square}}{R_{\square}n + R_{\square} + Z_0}\right|^2 \tag{24}$$

$$T = 4{Z_0}^2 \left|\frac{R_{\square}}{2R_{\square}Z_0 + {Z_0}^2}\right|^2 \tag{25}$$

Supplementary Note 4 - THz Incident on Substrate

The case where the THz beam is incident on the substrate first (with a graphene film on the backside) was investigated analytically with similar results as ref[6]. Contrary to the experimental setup used in this work, that is, where the THz beam is incident on the graphene film, if the THz beam is incident on the substrate side, the transmittance through the etalon remains the same (compared to incidence on the graphene side), but the reflectance and absorptance are different. The absorptance is plotted (with n = 3.41)

varying the graphene sheet resistance and kL varying from 0 – 2π in **Supplementary Fig. 5a** Although the values T, R, A, remain identical at half-wave resonance when kL = Nπ, at quarter-wave resonance, as clearly evident at kL = Mπ, where M is odd integer values, the total reflectance can decrease, resulting in increased absorbance. For this case (which is different from the experimental setup in this work) the absorptance values can be greater than 50% for n > 1. The peak absorption found at very low sheet resistance values calculated here were not apparent in similar plots in ref[6] (the sheet resistance where absorption begins to decrease was beyond the range analyzed), but here we emphasize that a sheet resistance dependent maximum absorption does indeed occur. The maximum absorptance, and the sheet resistance value at which it occurs can vary depending on the substrate index of refraction. These values were computed in **Supplementary Fig. 5b**. Here, it is obvious that the largest sheet resistance value for maximum absorbance occurs at 377/2 Ω/sq, when n = 1. Absorptance values greater than 90% can be achieved when n > 3 with the sheet resistance value required decreasing to values < 100 Ω/sq.

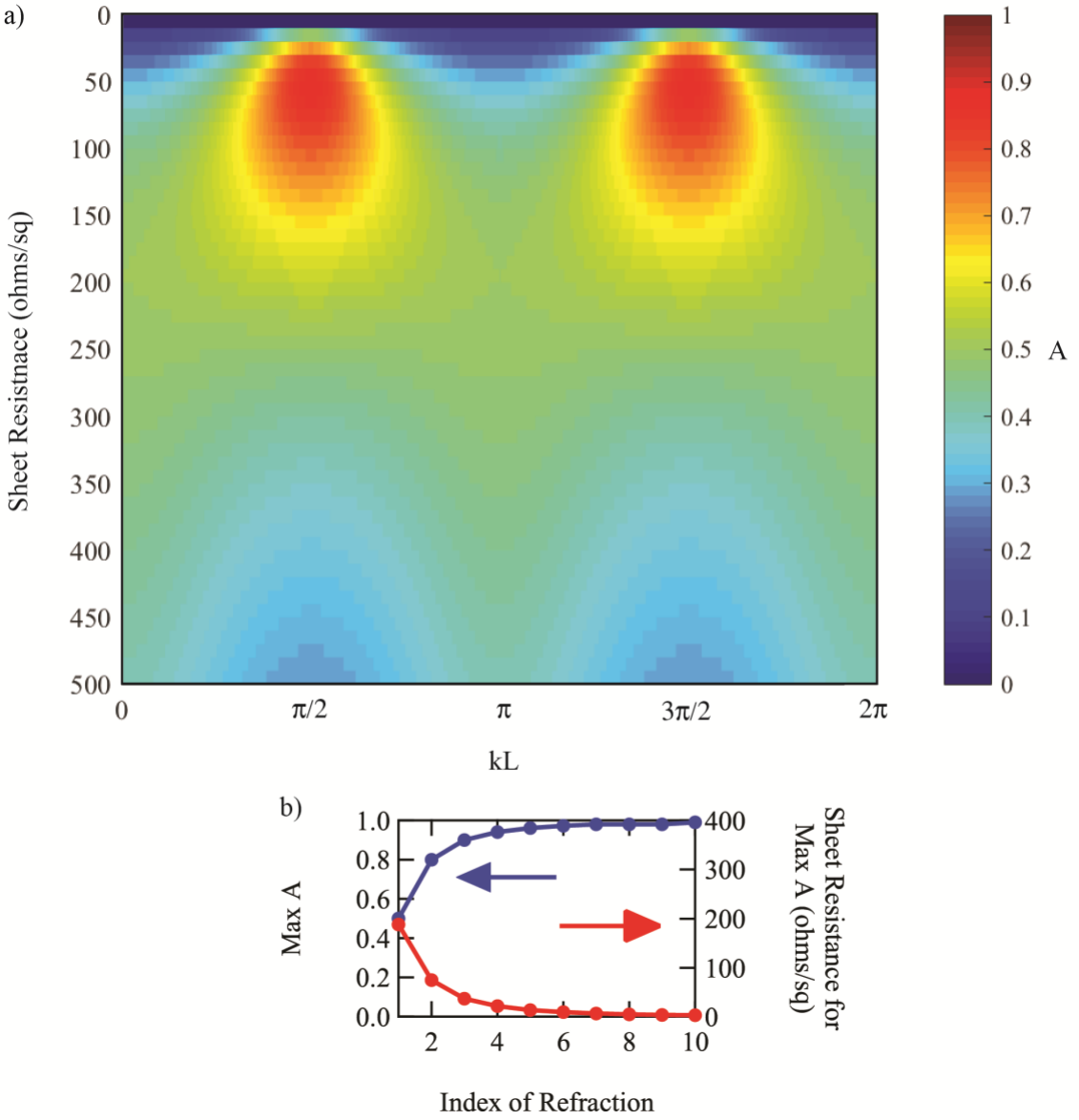

Supplementary Figure 5: a) The absorptance is plotted for the case when the THz beam is incident on the substrate (n = 3.41) side first as a function of the sheet resistance (ohms/sq) with kL varying from 0 – 2π. b) The maximum absorptance, and the sheet resistance required for various values of the index of refraction of the substrate.

T, R, A (Incidence on Substrate Side)

$$T = 4Z_0 \left| \frac{gn\left(n\sin(kL) - i\cos(kL)\right)}{(1+g+gn^2)Z_0\sin(kL) - i(1+2g)nZ_0\cos(kL)} \right|^2 \frac{2Z_0}{1+n^2-\cos(2kL)\,(n^2-1)} \quad (26)$$

$$R = \left| \frac{(1 + g - gn^2)\sin(kL) + incos(kL)}{(1 + g + gn^2)\sin(kL) - i(1 + 2g)ncos(kL)} \right|^2 \quad (27)$$

$$A = 4gZ_0^4 \left| \frac{n}{Z_0^2((1 + 2g)n\cos(kL) + i(1 + g + gn^2)\sin(kL)} \right|^2 \quad (28)$$

Supplementary Note 5 - Graphene Transfer onto ODTS SAM

CVD grown, monolayer graphene films are transferred onto an ODTS SAM on the SiO_2 substrate depicted in **Supplementary Fig. 6**. The ODTS SAM is vacuum deposited on the wafer prior graphene transfer. During the transfer step, BI can be introduced on the bottom of the film to intentionally dope the graphene. Scanning electron microscopy (SEM) imaging of the transferred graphene film was performed to determine the surface film quality following transfer, shown in **Supplementary Fig. 6b**. Although there are small topological variations, such as bumps and wrinkles created during the transfer process, we observe no detrimental defects (such as holes or tears) in the graphene film. As demonstrated in depletion curves shown in **Supplementary Fig. 7b-c**, graphene films transferred onto ODTS modified substrates exhibit a Dirac-point voltage ~ 22 Vg. This allows greater sensitivity while gating for modulation experiments.

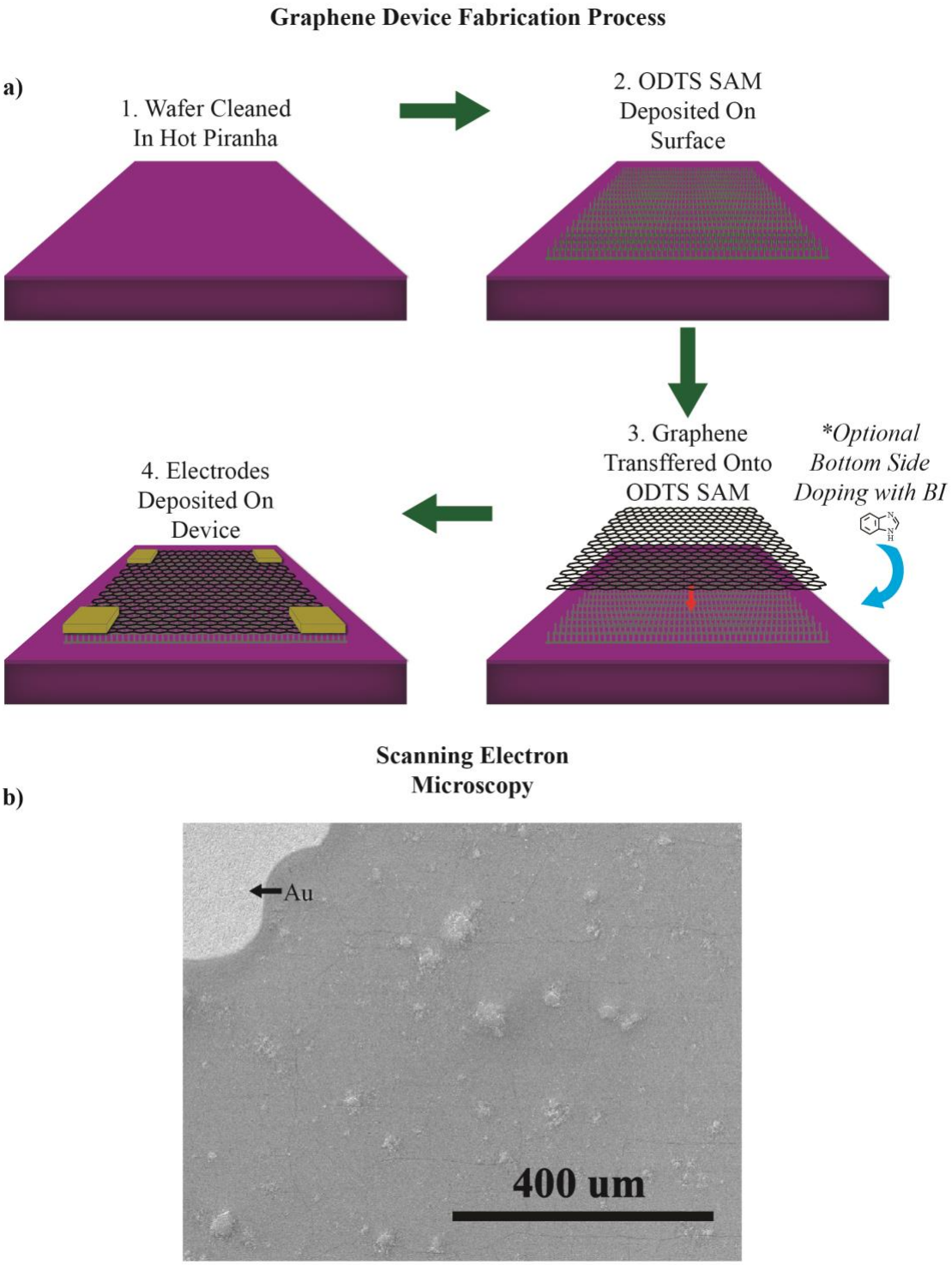

Supplementary Figure 6: a) Diagram of graphene transfer onto ODTS SAM. First a SiO_2 on high-resistivity Si substrate is cleaned in hot piranha solution. This step assists in the vacuum deposition of the ODTS SAM on the substrate surface. Graphene is then transferred using typical wet transfer protocol, with optional BI doping. After the graphene film is transferred and cleaned, electrodes are deposited for electrical measurement. b) SEM image of transferred graphene film. A gold electrode is seen in the top left corner, along with topological bumps and wrinkles from the transfer process.

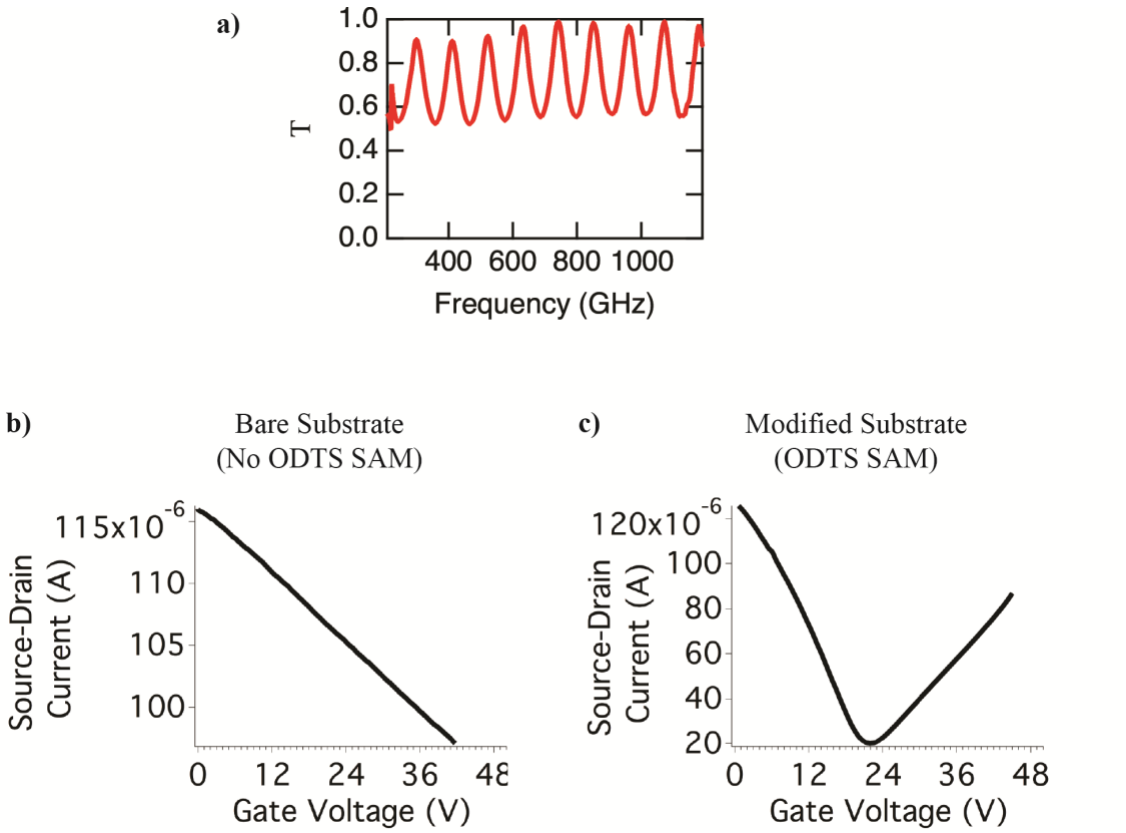

Supplementary Figure 7: a) Transmittance versus frequency of SAM layer on substrate. b) Depletion curve of graphene film on standard substrate without ODTS SAM modification. c) Depletion curve of graphene film on substrate with ODTS SAM modification. The Dirac-point voltage on ODTS SAM modified substrates is ~ 22 Vg, and improves the transconductance.

Supplementary Note 6 - SAM Absorption

Supplementary Fig. 7a shows the transmittance versus frequency of a substrate with a SAM modified surface. The THz transmittance (half-wave resonance) nearly reaches unity across the measured frequency range. In the most extreme circumstance, the transmittance is not completely lossless, but is nevertheless over 90%. This value corresponds to a sheet resistance value of ~ 3500 Ω/sq. Because the SAM resistance is in parallel with the graphene film, the large resistance of the SAM has limited effect when the graphene sheet resistance is low, and results in a difference of less than 15%. The influence of the SAM plays a more significant role when the graphene sheet resistance is comparable (such as when the graphene film is gated to ~ 2000 Ω/sq in **Fig. 3f**). This small absorption contribution from the SAM may potentially explain why the data point (d) deviates from the theory line in **Fig. 4c.**

Supplementary Note 7 - Electrical Modulation of Transmission

The broadband transmittance was measured for a single device at various gate voltages to test the performance as a THz modulator. The peak transmittance (centered at ~ 694 GHz) versus gate voltage is plotted on the same chart as the device resistance, shown below. On a different device (best), the depth of modulation (using +20 V_g and –7 V_g) versus frequency is displayed, and shows frequency variation of the DoM, with a

maximum value of ~ 52%. Variations may arise from inhomogeneous gating using the high resistivity silicon substrate. The use of a high resistivity substrate limits the device switching speed. Experimentally, we measured a modulation frequency of < 2 Hz.

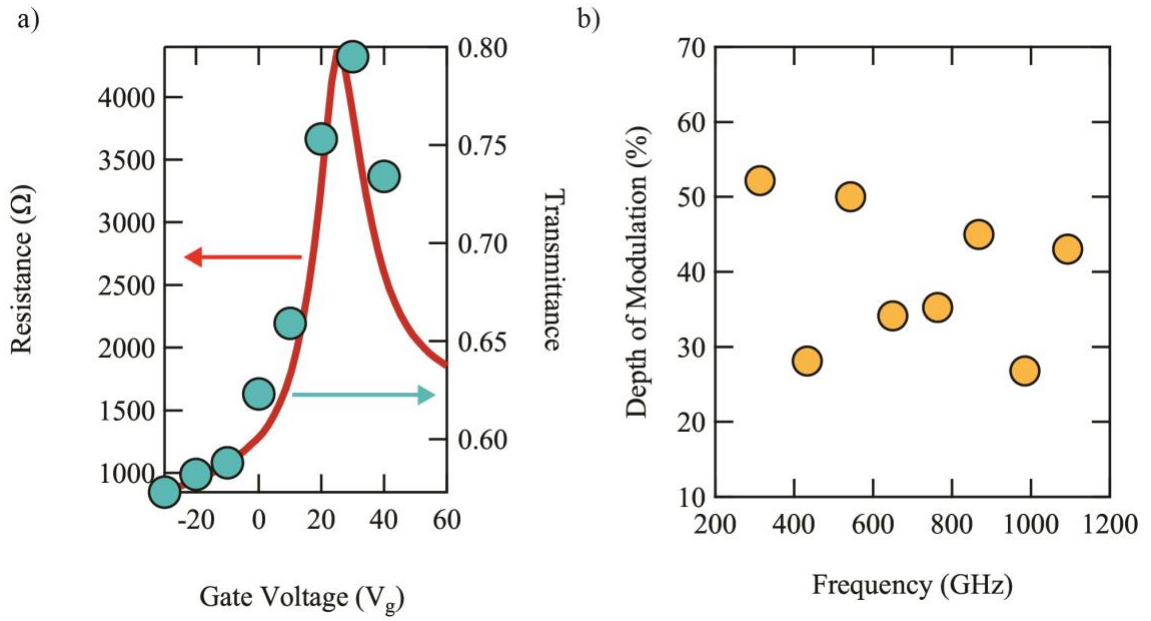

Supplementary Figure 8: a) The resistance versus gate voltage is plotted with the voltage dependent peak transmittance value (located at ~ 694 GHz). b) The depth of modulation of the transmittance peaks for a device under -7 and 20 Vg gate biasing. The maximum value (~ 52%) occurs around ~ 320 GHz, although significant modulation is seen across the broadband frequency range measured.

T_{max} is the maximum transmittance value at a peak of the spectra. Then the transmission variation is given by,

$$\frac{dT_{\max}}{T_{\max}} = -2Z_0\sigma_g \frac{1}{\varepsilon_s + \sigma_g Z_0 + 1}\frac{d\sigma_g}{\sigma_g} \tag{29}$$

where Z_0=377 Ω is the impedance of free space, ε_s is the dielectric constant of the Si substrate and σ_g is the conductance of graphene film. Assuming the device is mounted on a silicon substrate ($\varepsilon_s \approx 11.66$), the room temperature values from Banzerus et. al[7], (mobility ~ 145,000 cm^2/Vs) approaches 100% depth of modulation with only ~10 V on the gate.

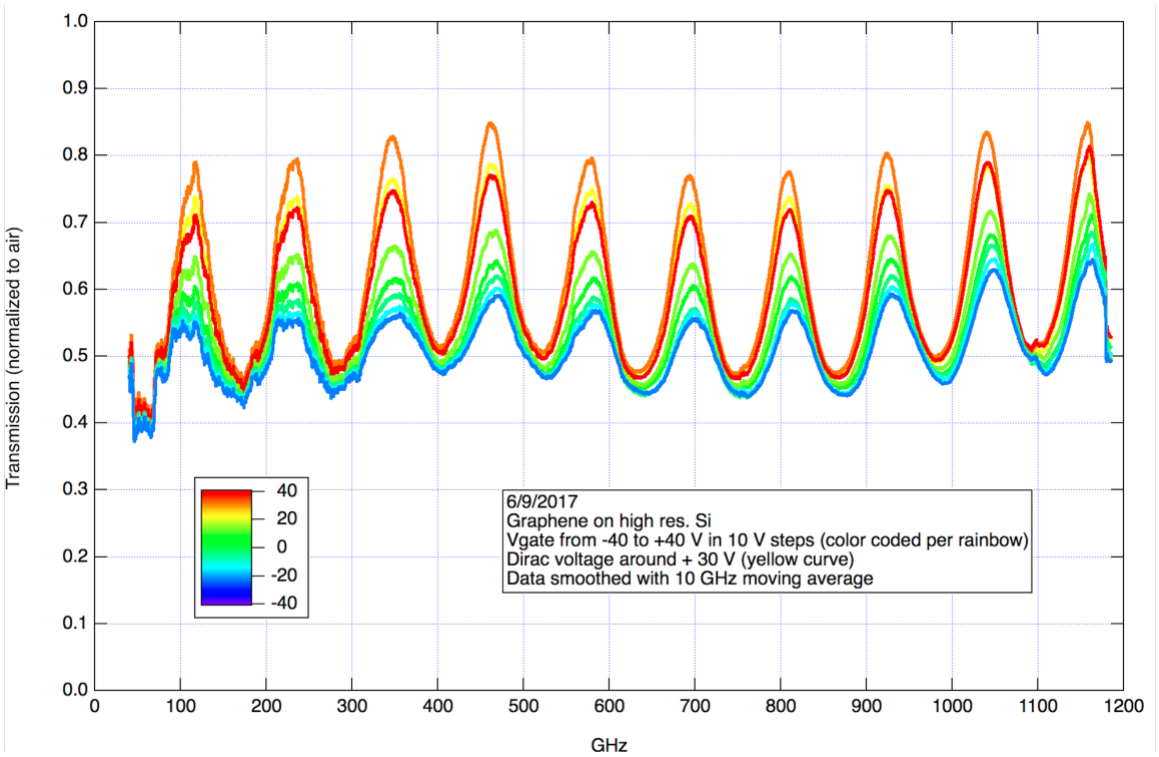

Supplementary Figure 9: Data independently confirming the broadband transmittance amplitude modulating as the graphene sheet resistance is varied (here, by applying a gate voltage on the Si layer) in a different lab using a Toptica Terascan frequency-domain THz spectrometer.

Supplementary Note 8 - Characterizing Doping of Graphene Films

We measured the depletion curve to investigate the effects of doping on the electrical properties of the graphene films. **Supplementary Fig. 10** shows the depletion curves of samples with and without BI doping on an ODTS substrate. After doping, the Dirac point voltage is subsequently shifted to > 48 Vg, indicative that the graphene film becomes hole doped. We found that with the use of BI doping, we could achieve a (zero gate biased) DC sheet resistance below the impedance of free-space. Even with BI doping, the sheet resistance values would vary from sample to sample. The sheet resistance differences from sample to sample could be explained by spatial variations in τ and E_F after doping.

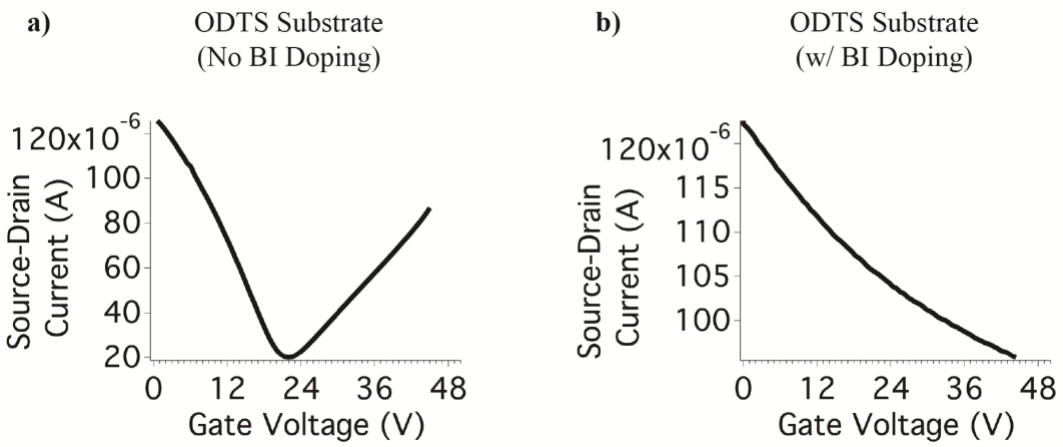

Supplementary Figure 10: Depletion curve data for two samples, with and without BI doping on ODTS substrates. Following doping with BI, the Dirac-point voltage becomes > 48 Vg.

To further investigate the effects of doping graphene, we employed Raman spectroscopy. Raman spectroscopy was performed using a Renishaw Invia Spectrometer with a 532 nm laser. Raman mapping was performed using the Streamline High Resolution (HR) mapping function over a 3 x 3 mm area with 60 um step size. The peak analysis and fitting was performed using the Wire 3.6 Renishaw software package. Mapping images are processed using Igor 6 plotting software.

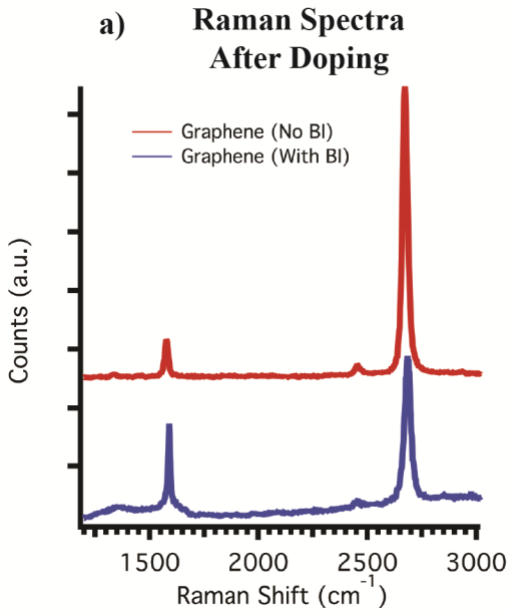

Supplementary Figure 11: Representative Raman spectra for samples with and without BI doping on an ODTS SAM modified substrate. Before doping, the [I]2D/[I]G ratio is much larger than after doping. Also the peak position of the g-peak becomes blue-shifted after doping.

Supplementary Fig. 11 shows representative Raman spectra of graphene samples with and without BI doping during transfer. Notably, after the addition of BI doping, we observe a decrease in the intensity ratio, [I]2D/[I]G. The [I]2D/[I]G ratio is known to

decrease when both the scattering and Fermi energy of the graphene film increase in magnitude[8–10], and thus provides a convenient parameter to assess the BI doping of graphene films. **Supplementary Fig. 12** shows the Raman mapping histograms and images of the [I]2D/[I]G with and without BI doping. We confirm the general trend (lower average in histrogram) of decreased [I]2D/[I]G ratio, but we also observe spatial variance of the graphene film after doping. This supports our belief that after doping, the graphene sheet resistance is not dominated merely by changes in E_F, but instead, by a combination of both E_F and τ. The extracted AC conductivity parameters (outlined below) further support this hypothesis, since under chemical doping, the lowest sheet resistance devices are not the largest E_F, but instead, a combination of moderate E_F and long τ.

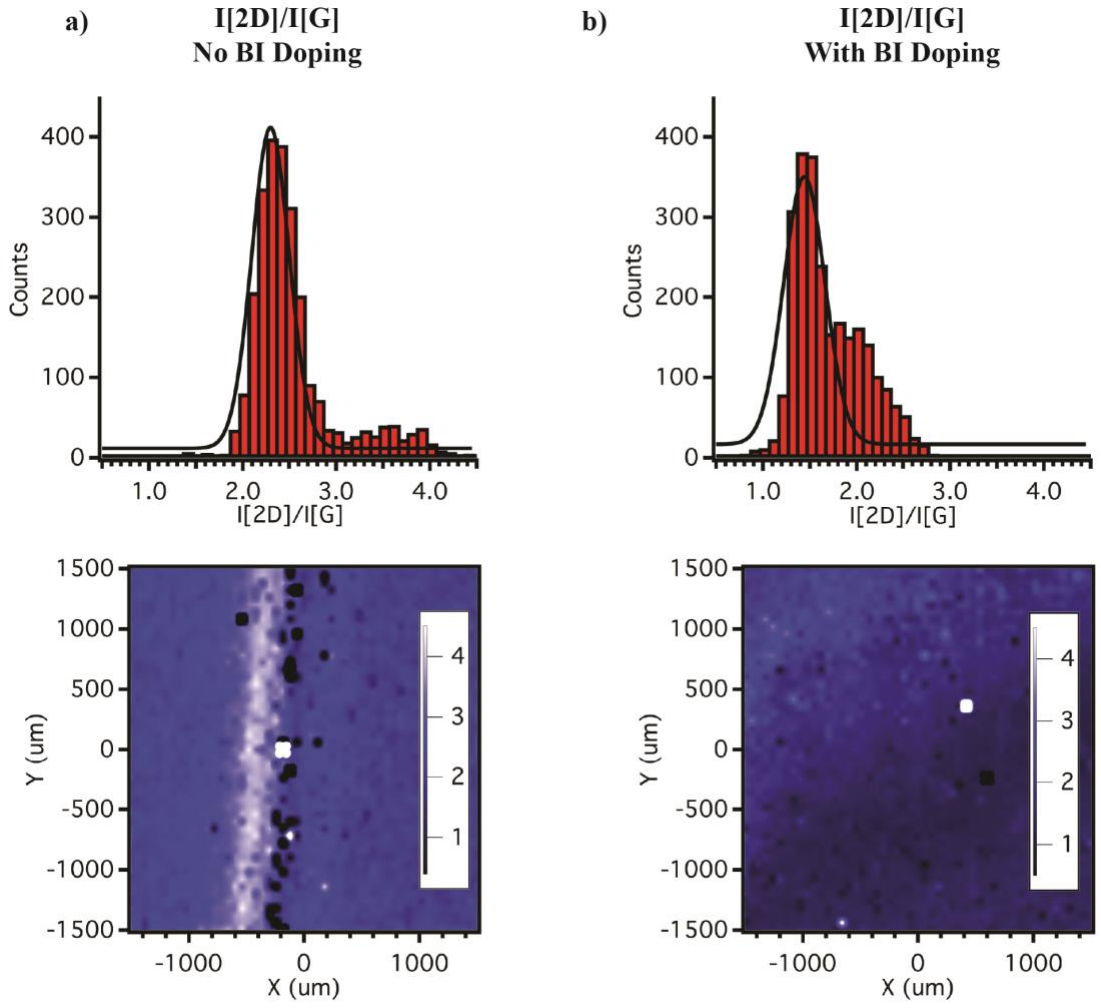

Supplementary Figure 12: Histograms and spatial mapping of [I]2D/[I]G ratio for two samples, with and without BI doping. After doping, the [I]2D/[I]G ratio decreases across the sample.

Supplementary Note 9 - Transmission Matrix Method for Calculating AC Conductance

The transmission matrix method is used[5] for calculating the conductance of graphene films from the transmittance measurement on a substrate of index of refraction, n, and

thickness, L. Assuming the THz beam is normally incident on the graphene surface, the transmittance, $T = |S_{21}|^2$

$$S_{21} = \frac{t_1 t_2 \exp(-ik_s L)}{1 + r_1 r_2 exp(-2ik_s L)} \tag{30}$$

where k_s is the wave vector inside the substrate, and is equal to $k_s = 2\pi\sqrt{\varepsilon_s}/\lambda$. ε_s is the dielectric constant of the substrate, silicon, and λ, is the free-space wavelength. For devices on a silicon substrate, $n = \sqrt{\varepsilon_s}$, with $\varepsilon_s \approx 11.66$ in the THz frequencies. r_1, and t_1, are the coefficients of reflectance and transmittance at the air-Si interface, while r_2, and t_2, are the coefficients of reflectance and transmittance at the Si-graphene/graphene-air interface. These are given by,

$$r_1 = \frac{1 - \sqrt{\varepsilon}_s}{1 + \sqrt{\varepsilon}_s} \tag{31}$$

$$t_1 = \frac{2}{1 + \sqrt{\varepsilon}_s} \tag{32}$$

$$r_2 = \frac{\sqrt{\varepsilon}_s - (\sqrt{\varepsilon}_g + 1)}{\sqrt{\varepsilon}_s + (\sqrt{\varepsilon}_g + 1)} \tag{33}$$

$$t_2 = \frac{2\sqrt{\varepsilon}_s}{\sqrt{\varepsilon}_s + (\sqrt{\varepsilon}_g + 1)} \tag{34}$$

The graphene dielectric constant is a complex value, $\varepsilon_g = Re\{\varepsilon_g\} + iIm\{\varepsilon_g\}$. The complex sheet admittance is computed by,

$$\sigma_g = \frac{\sqrt{\varepsilon_g}}{Z_0} \tag{35}$$

where $Z_0 = 377\ \Omega$ is the free-space impedance.

Each transmittance peak (consisting of a maximum, and two minimum values) is fitted to calculate the real and imaginary admittance value using a least squares fit procedure. During fitting, the substrate thickness, L, is adjusted for each device being analyzed.

Supplementary Note 10 - Comparison Plot

We now discuss the relationship of this work to prior work on graphene in the THz domain. **Supplementary Fig. 13** shows the range of conductance versus frequency for other monolayer graphene devices previously measured in the literature. Each trend line is plotted using equations (1) and (2), using data points supplied from each reference. The labeled and colored hashed (solid) regions (lines) indicate frequency domain

measurements, whereas the transparent grey regions (lines) are for time-domain systems. The frequency range measured for this paper is one of the broadest (with 500 MHz spectral resolution) investigating graphene-THz coupling, complemented by an extensive range of conductance values, including the achievement of surpassing the free-space impedance threshold.

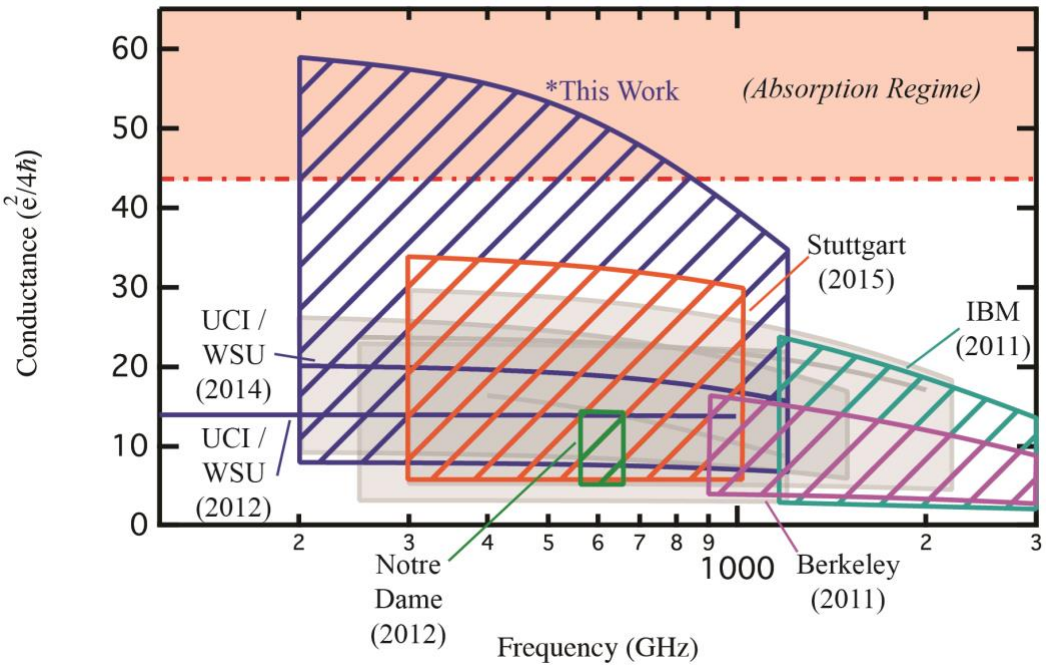

Supplementary Figure 13: Conductance versus frequency range of other graphene devices in the literature. Hashed regions indicate frequency domain systems, while the transparent grey regions show time-domain measurements.

The table below shows both the conductance range and the frequency range of the references used in **Supplementary Fig. 13**. The optical conductance values are those measured and reported from each reference, and τ and E_F are estimated to reflect this value. In reference 8, τ is defined as $\tau = \hbar/\Gamma$, where τ is the scattering time, $\hbar$ is the Planck constant, and Γ is the phenomenological scattering parameter, whereas in our calculations, τ is defined as, $\tau = \hbar/2\Gamma$.

Extracted Drude Parameters

Device Measured	DC Sheet Resistance	Modulation Type	τ (fs)	E_F (meV)
Fig. 3d	~ 2000 Ω/sq	Electrical (+20 V_g)	44	105
Fig. 3e	~ 515 Ω/sq	Electrical (-7 V_g)	99	209
Fig. 3f	~ 515 Ω/sq	Chemical Doping	28	583
Fig. 3g	~ 373 Ω/sq	Chemical Doping	74	339
Fig. 3h	~ 250 Ω/sq	Chemical Doping	111	284

Supplementary Table 1: Table of DC resistance, and the extracted E_F and τ values for both electrical and chemical modulation of devices measured in the main text.

Main Text Reference	Frequency Range (GHz)	Measurement Type	Optical Conductance Range ($e^2/4\hbar$)	Estimated to Equal Optical Conductivity	
				τ (fs)	E_F (meV)
Yan et al. #6	1190 -	Frequency Domain (FTIR)	23.7	*23	560
Horng et al. #7	900 -	Frequency Domain (FTIR)	1.9 – 16.09	55	170
Rouhi et al. #8	100 - 1000	Frequency Domain	14.07	50	150
Zhang et al. #9	200 -1200	Frequency Domain	20.63	72	150
Sensale – Rodriguez et al. #10	560 - 660	Frequency Domain	3.28 - 14.8	50	153
Ren et al. #12	100 - 2200	Time Domain	5 - 27.41	50	252
Cervertti et al. #13	300 - 1000	Frequency Domain	3.94 - 36.18	123	157
Min Woo et al. #14	250 - 2100	Time Domain	23.87	50	254
Maeng et al. #15	200 - 1500	Time Domain	5 - 27.09	48.8	295
Buron et al. #16	250 - 1200	Time Domain	3.2 - 23.02	50	246
Mics et al. #18	400 - 1200	Time Domain	19.73	140	70

Supplementary Table 2: Table of frequency range, measurement domain, and achieved conductance range for each reference used in Supplemental Fig. 13.

Supplementary Note 11 - Maximum Absorptance (Incidence on Graphene Side)

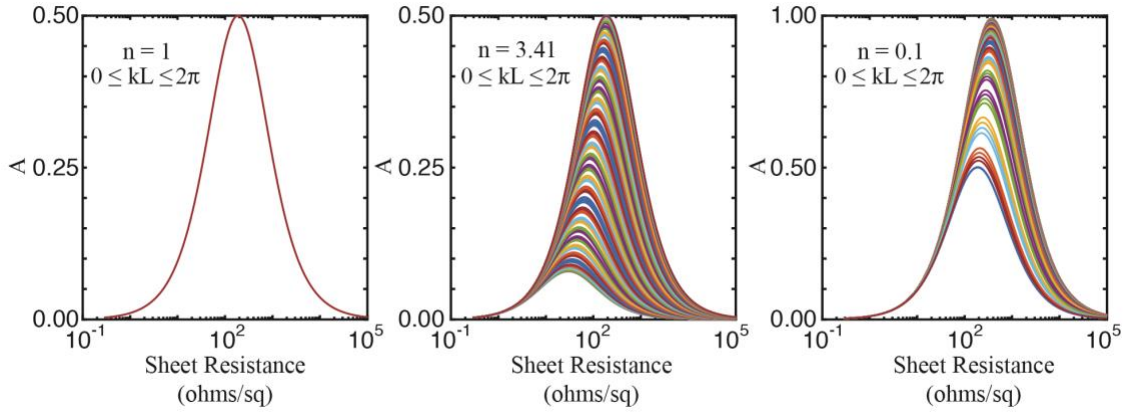

Supplementary Figure 14: The absorption versus sheet resistance for 3 different values of n, while varying kL from 0 to 2π.

The absorptance versus sheet resistance is plotted using the general absorptance **Eq. (7) – (9)** in the case where the THz beam is incident on the graphene side for three values of the n (substrate index of refraction), while varying kL from 0 to 2π.When n = 1 the maximum absorptance is 50%. The maximum absorptance value is also 50% with when n = 3.41 (substrate used in this work) at the half-wave resonance values (kL = Nπ), with a minimum value of ~ 8% in the quarter-wave resonance case. Although **Eq. (7) – (9)** can yield absorptance values greater than 50%, this is only satisfied for values of n < 1, which is not considered in this manuscript, but nonetheless useful for cases such as metamaterials. Hence, 50% is considered the maximum for incidence on the graphene side.

THz Mobility

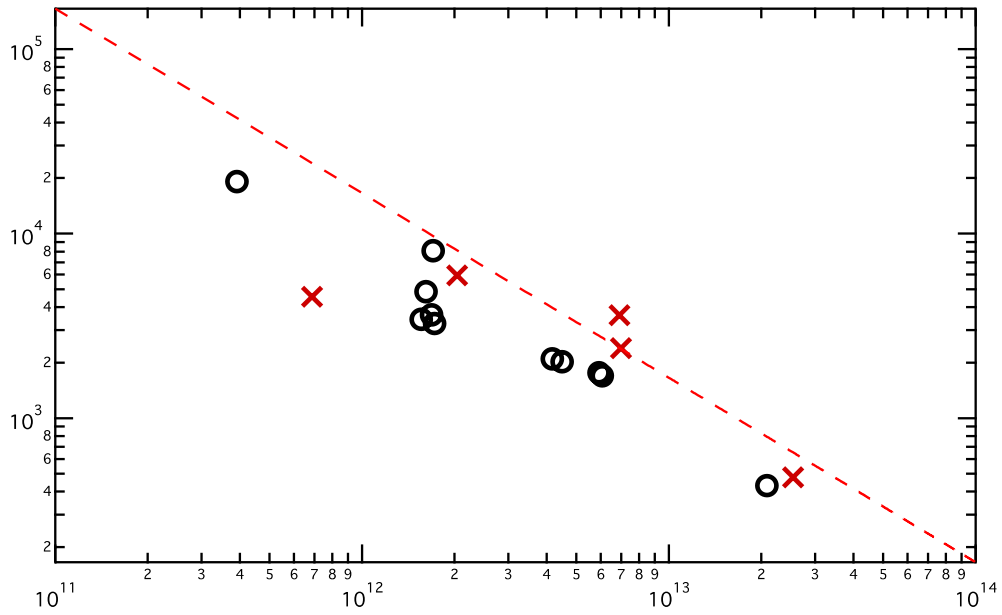

Supplementary Figure 15: The mobility versus carrier density calculated[11] using the scattering time and optical conductivity values from this work, and those reported in Supplementary Table 2. The dotted line shows the 377 Ω threshold.

Supplementary Note 12 - Substrate Thickness

Device Measured	Fig. 3c	Fig. 3d	Fig. 3e	Fig. 3f	Fig. 3g	Fig. 3h
Thickness	395 μm	395 μm	395 μm	398 μm	382 μm	401 μm
Peak-to-peak Spacing	113.48 ± 1.51 GHz	112.04 ± 1.15 GHz	113.23 ± 3.55 GHz	110.74 ± 1.32 GHz	115.50 ± 2.88 GHz	109.64 ± 4.97 GHz

Supplementary Table 3: Table of the effective thickness used for calculation for each device. Also listed are the peak-to-peak spacing averages of the experimental data for each device.

The effective thickness of each device is held constant during calculation and fitting using the values listed above. The peak-to peak spacing of each transmittance peak of all devices were analyzed, and the average values are also listed in **Supplementary Table 3**. Small deviations in the peak-to-peak spacing are apparent. This variation could be due to the common issue collimating the THz beam, where, when the device is not absolutely parallel leads to a spread in the effective substrate thickness. Nonetheless, the peak-to peak spacing agrees with the different effective thickness from the various device. Furthermore, the instrument used is a fiber-based frequency domain photomixing spectrometer; insertion of a sample into the THz beam may shift the interference fringes on the THz arm, leading to a slight off-balance with respect to the optical arm. Therefore, some irregular frequency points in the measured transmittance may be contributed by "instrument drift". To mitigate the experimental uncertainty from both the instrument drift and beam collimation, post experimental data analysis was employed. Here, we performed fitting to every individual interference pattern around every peak which contains up to hundreds of frequency-transmission points. From the extracted conductance at those individual peaks, we obtain E_F and τ with the Drude model, and compare the calculated DC conductance to the measured DC value, as seen in **Fig. 4a-b**. Here, we find that the two values agree with each other, and supports the reliability of our data.

Supplementary Note 13 - Imaginary Contributions

A Drude-like roll off is expected for frequencies greater than $1/\tau$, as the imaginary contributions become significant, especially when τ is long. During fitting of the measured transmittance peaks, both the real and imaginary contributions were calculated. However, when fitting for τ and E_F only the real contribution is used. Because the Kramers-Koenig relation relates the real and imaginary contributions, a fit on only the real yields valid results[5]. **Supplementary Fig. 16** shows the real and imaginary values calculated, and the calculated Drude trend from the (real part) fitted E_F and τ values for the best device of 250 Ω/sq. The predicted line generally agrees the measured conductance trend. Though the error of the imaginary fit is larger than that on the real part, this error can potentially be improved from a direct measurement of the phase. This would improve the fitting of τ, and would provide a more accurate range of the Drude-shaped roll off ($\omega \sim 1/\tau$). For our best device (~ 250 Ω/sq), the high frequency

transmittance peaks start to deviate from the predicted trend (when using the measured DC sheet resistance as the real part, ignoring imaginary contributions), suggesting significant contributions from the imaginary. The frequency dependent amplitude deviation is generally not observed in other devices.

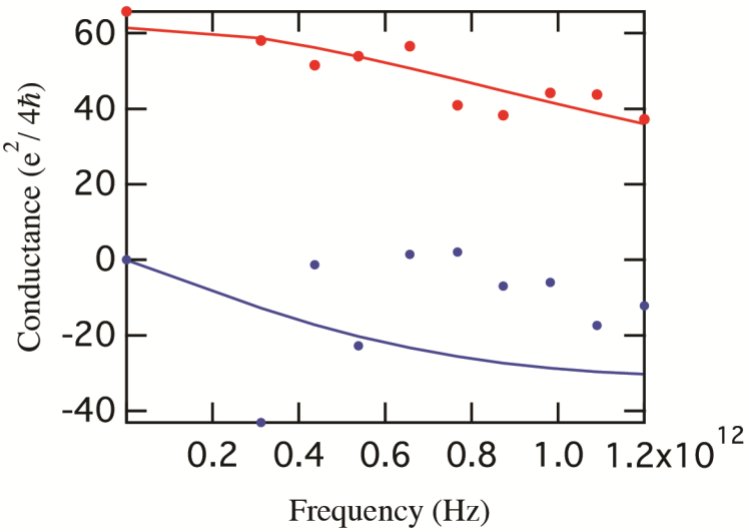

Supplementary Figure 16: The real (red) and imaginary (blue) contributions of the AC admittance calculated by fitting the broadband transmittance data for the best device of 250 Ω/sq. Using the real values, the Drude parameters were calculated, and the Drude prediction is plotted as solid lines.

Supplementary References

1. Dressel, M. & Gruner, G. *Electrodynamics of Solids: Optical Properties of Electrons in Matter*. (Cambridge university press, 2002).
2. Brown, E. R., Zhang, W. D., Chen, H. & Mearini, G. T. THz behavior of indium-tin-oxide films on p-Si substrates. *Appl. Phys. Lett.* **107,** 91102 (2015).
3. Pozar, D. M. *Microwave Engineering*. (J. Wiley, 2005).
4. Woltersdorff, W. Uber die optischen Konstanten dunner Metallschichten im langwelligen Ultrarot. *Zeitschrift fur Phys.* **91,** 230–252 (1934).
5. Zhang, W., Pham, P. H. Q., Brown, E. R. & Burke, P. J. AC conductivity parameters of graphene derived from THz etalon transmittance. *Nanoscale* **6,** 13895–9 (2014).
6. Zanotto, S. *et al.* Coherent absorption of light by graphene and other optically conducting surfaces in realistic on-substrate configurations. *APL Photonics* **2,** 16101 (2017).
7. Banszerus, L. *et al.* Ultrahigh-mobility graphene devices from chemical vapor deposition on reusable copper. *Sci. Adv.* **1,** e1500222 (2015).
8. Ferrari, A. C. *et al.* Raman Spectrum of Graphene and Graphene Layers. *Phys. Rev. Lett.* **97,** 187401 (2006).
9. Das, A. *et al.* Monitoring dopants by Raman scattering in an electrochemically top-gated graphene transistor. *Nat. Nanotechnol.* **3,** 210–215 (2008).
10. Lee, W. H. *et al.* Control of Graphene Field-Effect Transistors by Interfacial Hydrophobic Self-Assembled Monolayers. *Adv. Mater.* **23,** 3460–3464 (2011).
11. Tan, Y. W. *et al.* Measurement of scattering rate and minimum conductivity in graphene. *Phys. Rev. Lett.* **99,** 246803 (2007).